A 5.3-minute pulsing white dwarf in a binary detected from radio to X-rays

Ingrid Pelisoli[1*], T. R. Marsh[1], David A. H. Buckley[2,3,4], I. Heywood[5,6,7], Stephen. B. Potter[2,8], Axel Schwope[9], Jaco Brink[2,3], Annie Standke[9,10], P. A. Woudt[3], S. G. Parsons[11], M. J. Green[12], S. O. Kepler[13], James Munday[1,14], A. D. Romero[13], E. Breedt[15], A. J. Brown[11], V. S. Dhillon[11,16], M. J. Dyer[11], P. Kerry[11], S. P. Littlefair[11], D. I. Sahman[11], and J. F. Wild[11]

[1]Department of Physics, University of Warwick, Coventry, CV4 7AL, UK
[2]South African Astronomical Observatory, PO Box 9, Observatory, 7935, Cape Town, South Africa
[3]Department of Astronomy, University of Cape Town, Private Bag X3, Rondebosch 7701, South Africa
[4]Department of Physics, University of the Free State, PO Box 339, Bloemfontein 9300, South Africa
[5]Astrophysics, Department of Physics, University of Oxford, Keble Road, Oxford, OX1 3RH, UK
[6]Department of Physics and Electronics, Rhodes University, PO Box 94, Makhanda 6140, South Africa
[7]South African Radio Astronomy Observatory, 2 Fir Street, Observatory 7925, South Africa
[8]Department of Physics, University of Johannesburg, PO Box 524, Auckland Park 2006, South Africa
[9]Leibniz-Institut für Astrophysik Potsdam (AIP), An der Sternwarte 16, 14482 Potsdam, Germany
[10]University of Potsdam, Institute for Physics and Astronomy, Karl-Liebknecht-Straße 24/25, 14476 Potsdam, Germany
[11]Department of Physics and Astronomy, University of Sheffield, Sheffield, S3 7RH, United Kingdom
[12]School of Physics and Astronomy, Tel-Aviv University, Tel-Aviv 6997801, Israel
[13]Instituto de Física, Universidade Federal do Rio Grande do Sul, 91501-970 Porto Alegre, RS, Brazil
[14]Isaac Newton Group of Telescopes, Apartado de Correos 368, E-38700 Santa Cruz de La Palma, Spain
[15]Institute of Astronomy, University of Cambridge, Madingley Road, Cambridge CB3 0HA, UK
[16]Instituto de Astrofísica de Canarias, E-38205 La Laguna, Tenerife, Spain
[*]ingrid.pelisoli@warwick.ac.uk

White dwarf stars are the most common stellar fossils. When in binaries, they make up the dominant form of compact object binary within the Galaxy and can offer insight into different aspects of binary formation and evolution. One of the most remarkable white dwarf binary systems identified to date is AR Scorpii (henceforth AR Sco). AR Sco is composed of an M-dwarf star and a rapidly-spinning white dwarf in a 3.56-hour orbit. It shows pulsed emission with a period of 1.97 minutes over a broad range of wavelengths, which led to it being known as a white dwarf pulsar. Both the pulse mechanism and the evolutionary origin of AR Sco provide challenges to theoretical models. Here we report the discovery of the first sibling of AR Sco, J191213.72−441045.1 (henceforth J1912−4410), which harbours a white dwarf in a 4.03-hour orbit with an M-dwarf and exhibits pulsed emission with a period of 5.30 minutes. This discovery establishes binary white dwarf pulsars as a class and provides support for proposed formation models for white dwarf pulsars.

The white dwarf pulsar AR Sco is **detected over a broad range of wavelengths, from radio[1] to X-rays[2].** The spin-down of its rapidly-rotating white dwarf **provides enough energy to power the pulses[3]**, but the exact driving mechanism is not fully understood. **Unlike in neutron star pulsars, where no companion is required, binarity seems to play an important role in AR Sco's pulses.** The observed periodicity of 1.97 min is consistent with a reprocessed frequency, the beat frequency between the 1.95 min spin period of the white dwarf and the 3.56-hour orbital period. This suggests that interaction between the white dwarf and the M-dwarf is behind the pulse mechanism. Proposed models **for the origin of emission** include the surface or

coronal loops of the M-dwarf companion[4], the magnetosphere of the white dwarf[5,6], close to the surface of the white dwarf[7], or through an associated bow shock[8].

One of the main challenges to explain AR Sco is to reconcile the present fast spin-down rate with the rapid spin of the white dwarf. The observed spin period requires previous spin-up via mass accretion. That is because non-interacting main sequence stars slow down their rotation as they age[9], resulting in rotation periods of the order of days for their white dwarf remnants[10,11]. Only white dwarfs in cataclysmic variables have rotation periods comparable to AR Sco, which is explained by angular momentum gain via mass accretion from the companion[12]. However, whereas the spin-down rate of AR Sco suggests that a strong magnetic field of 50–100 MG provides the synchronising torque[4], the rapid spin can only be achieved with typical mass transfer rates **via Roche-Lobe overflow** if the magnetic field is much smaller (~ 1 MG)[13]. With the strong magnetic field, a very large mass transfer rate of **up to** $\dot{M} \sim 10^{-4}\,\mathrm{M}_{\odot}\,\mathrm{yr}^{-1}$ would be required to achieve a 1.95 min spin[14]. This rate is well beyond the ordinary M-dwarf companion seen in AR Sco, and is 10^5 times greater than the rates typical of similar binaries[15]. **Accretion via diamagnetic blobs could allow for lower rates[16], but the origin of the strong magnetic field in AR Sco would remain unexplained.**

A solution to this conundrum has recently been put forward[17]. In the proposed model, the white dwarf in AR Sco was originally non-magnetic, allowing for straightforward accretion-driven spin-up. When crystallisation started to occur in the core of the cooling white dwarf, strong density stratification combined with convection created the conditions for a dynamo, generating the magnetic field[18,19]. With a strong enough field, the rapid transfer of spin angular momentum into the orbit causes the binary to detach and mass transfer to **briefly** cease, leading to a **rare** system such as AR Sco. **After a few millions of years, the system comes into contact again due to reduced magnetic braking and gravitational radiation, giving origin to a rapidly rotating accreting magnetic white dwarf.** As well as addressing the issue of forming a system like AR Sco, the proposed model also provides a solution to a long-lasting problem in the field of white dwarf binaries: the discrepancy between the fraction of magnetic white dwarfs in detached versus accreting binaries. Strongly magnetic white dwarfs are nearly absent in detached white dwarf binaries[20,21], whereas more than one third of those in accreting systems are magnetic[22]. The dynamo mechanism can naturally explain that, as magnetic accreting white dwarfs are typically old and cool enough to have been crystallised, and they have been spun up by accretion to short periods such that the dynamo effect is intensified.

An important aspect of this promising rotation- and crystallisation-driven dynamo model is that it suggests that binary white dwarf pulsars like AR Sco are a possible stage in the evolution of accreting magnetic white dwarfs. Though the timescales in the model cannot be precisely established, given the existence at the time of only one object available to calibrate it, the properties of AR Sco itself suggest that other binary white dwarf pulsars should exist. First, considering its distance to Earth of only 117 pc, more objects should be expected at larger volumes; second, its spin-down rate suggests that the lifetime in such a stage is of millions of years[3]. **This model also predicts that the white dwarfs in AR Sco-like systems should be cool enough to have crystallised, and that their companions should be close to Roche-lobe filling. Finally, based on the observed population of accreting systems, the model also predicts pulsars to have orbital periods in the range of three to**

five hours.

Although a few systems have been proposed as potential white dwarf pulsars[23–25], none of them have been confirmed, and as such AR Sco has remained unique even after six years of its discover. To address the lack of other systems that could confirm binary white-dwarf pulsars as an evolutionary stage and help to constrain the timescales and predictions of the rotation- and crystallisation-driven dynamo model, we performed a targeted search for binary white-dwarf pulsars. We searched for objects showing observational properties similar to AR Sco, in particular non-thermal infrared colours, variability, and location in the *Gaia* colour-magnitude diagram[26]. A few tens of candidates were identified, over two thirds of which have already been followed-up. Follow-up high-speed photometry with ULTRACAM[27] on the 3.58 m New Technology Telescope (NTT) revealed that one of the candidates, J1912−4410, shows strong pulses with a period of 5.3 min, during which the *g*-band flux increases by up to a factor of four. Independently, J1912−4410 was detected as an X-ray source with *eROSITA* during its all-sky surveys[28] and identified as a compact binary candidate due to its combined optical (as seen by *Gaia*) and X-ray properties. These discoveries prompted further follow-up.

We obtained ULTRACAM photometry on a total of five nights. We also obtained photo-polarimetry on five nights with the High speed Photo-Polarimeter (HIPPO[29]) mounted on the 1.9 m telescope at the South African Astronomical Observatory (SAAO). Additionally, we retrieved archival photometry from the Transiting Exoplanet Survey Satellite (TESS)[30], the Asteroid Terrestrial-impact Last Alert System (ATLAS)[31], the Catalina Real-time Transient Survey (CRTS)[32], and the All-Sky Automated Survey for Supernovae (ASAS-SN)[33]. Spectroscopy was firstly obtained with the Goodman spectrograph[34] at the 4.0 m Southern Astrophysical Research (SOAR) telescope and with the 1.0 m telescope at SAAO, which allowed us to confirm that J1912−4410 showed similar spectral characteristics to AR Sco: an optical spectrum displaying a blue continuum added to the red spectrum of an M-type dwarf, with strong Balmer and neutral helium lines in emission (see Extended Data Figure 1). Fast frame-transfer spectroscopy was obtained with the 9.2 m Southern African Large Telescope (SALT), and full orbital coverage was obtained with X-shooter[35] at the 8.2 m Very Large Telescope (VLT). Further X-ray data were obtained with *XMM-Newton*, after the detection with *eROSITA* which demonstrated the feasibility of such observations. Radio imaging follow-up observations were carried out using MeerKAT's L-band receivers (856–1712 MHz). Further details on the observations and data reduction are given in the Methods section.

The TESS photometry revealed a dominant frequency at 5.948136(13) cycles/d. Radial velocities obtained for the M-dwarf from the X-shooter spectra show that this frequency corresponds to the orbital period of the binary, of 0.16811989(36) days (Fig. 1). **The photometric orbital modulation is asymmetric, which cannot be explained by reflection alone. This is likely due to contribution from non-thermal emission, with the asymmetry arising either due to more power being dissipated in the leading face of the M-dwarf, or due to a misaligment between spin and orbit axis, leading to phase-dependent dissipation rate[4].** The observed radial velocity amplitude depends on the spectral line, reflecting the fact that the emission or absorption features originate in different locations on the M-dwarf. We used the difference between the amplitude measured the from NaI absorption lines (8183 and 8195 Å), inherent to the M-dwarf photosphere, and the Balmer emission lines, which

originate on the irradiated side facing the compact object, to constrain the Roche geometry of the system (details in the Methods section). Additionally, we imposed an upper mass limit equal to the Chandrasekhar mass for the compact object, requiring it to be a white dwarf due to its spin period, which is more than a factor of four longer than any confirmed neutron star pulsar[36]. With this upper mass limit, a mass ratio of $q = M_2/M_1 > 0.3$[1] is needed for the origin of both emission and absorption features to fit within the Roche lobe of the M-dwarf (see Extended Data Figure 2). The observed centre-of-mass radial-velocity amplitude of the M-dwarf can only be explained for this range of q if the mass of the white dwarf is $M_1 > 0.32$ M$_\odot$. An upper limit to the M-dwarf mass can be obtained by requiring it to fit within its Roche lobe, where it would have a mean density determined by the orbital period[37]. We obtain $M_2 < 0.42$ M$_\odot$. The spectral type of the M-dwarf is M4.5$\pm$0.5 (see Methods), suggesting a mass of ≈ 0.3 M$_\odot$, much below the Roche-lobe filling upper limit. This implies that either the M-dwarf is not close to Roche lobe filling, unlike AR Sco[38], or that the system is seen at low inclination, resulting on a lower observed difference between the velocities of NaI and the Balmer lines due to projection along the line of sight. In fact, we find that our mass constraints imply a maximum inclination for the system of $i = 37°$, favouring the latter interpretation (see Extended Data Figure 2, panel b). Combining these constraints with the *Gaia* data release 3 distance of 237 ± 5 pc[39], which allows us to constrain the radius of the M-dwarf from spectral fitting, we estimate the system masses to be $M_1 = 1.2 \pm 0.2$ M$_\odot$ and $M_2 = 0.25 \pm 0.05$ M$_\odot$ (see Extended Data Figure 3)**, with the companion potentially filling over 90% of its Roche lobe. The white dwarf temperature cannot be determined due to the lack of contribution of the white dwarf in the optical wavelengths, but the upper limit derived from the lack of visible features is consistent with at least the onset of crystallisation (details in the Methods section).**

The amplitude spectra computed from our fast-speed photometry reveal several peaks separated by multiples of the orbital frequency (Fig. 2). We interpret the dominant peak of 270.55038(7) cycles/day as the spin frequency of the white dwarf (more details in the Methods section), corresponding to a spin period of 319.34903(8) s. Our short baseline of under 5 months reveals no detectable spin period change, which is unsurprising: if J1912−4410 shows a similar spin-down rate to AR Sco, the expected change in the spin period over our baseline would be of the order of 10^{-9} s, much smaller than the precision in our derived spin period. The pulses are detected in all observed frequencies from radio to X-rays, showing that, like AR Sco, J1912−4410 shows a broad spectral energy distribution (SED) that can be orders of magnitudes brighter than the thermal emission from its component stars, particularly at radio and X-ray wavelengths (Fig. 3). Integrating the SED shown in Fig. 3 and using the *Gaia* distance, we find the bolometric luminosity to be $\sim 10^{33}$ erg/s, well in excess of the total stellar luminosity of $\sim 10^{31}$ erg/s. The excess is even higher than in AR Sco, potentially suggesting a faster spin-down rate, or another source of energy such as accretion (see below).

We interpret the mechanism behind the broad-band pulsed emission to be the same as in AR Sco: synchrotron radiation. A synchrotron emission source locked to the rotating frame of the white dwarf, which receives an injection of electrons as the magnetic field of the white dwarf sweeps past the companion, can reproduce the observed pulse profile, as illustrated in

[1] We use the subscripts 1 and 2 to refer to parameters describing the white dwarf and the M-dwarf, respectively.

Fig. 4 (details in the Methods section). The electrons are accelerated to relativistic speeds **due to magnetic reconnection**, resulting in beamed synchrotron emission. The pulsed emission show a complex shape that varies with orbital phase and, to some extent, over time (see Extended Data Figure 4). At least two components can be identified. First, a narrow component which is particularly dominant in radio, where its full width at half maximum (FWHM) is less than 4 s. This narrow pulse is also seen in the optical, over a much broader second component that dominates both optical and X-rays (see middle panels in Fig. 2). The broader component seen in all wavelengths is likely the result of synchrotron beaming coming at each spin cycle **when the magnetic field of the white dwarf sweeps past the companion**. The narrow pulses that dominate in radio are reminiscent of neutron star pulsar variability and unlike the broad radio pulses observed for AR Sco[1]. Perhaps the low inclination of J1912−4410 provides a better view of a magnetic pole, which could be emitting in a similar manner to neutron star pulsars**, with very narrow pulses that are directly detected. The phase lag between the two pulses suggests different origins in the system, or at least distinct optical path lengths depending on energy.**

At least one feature seen both in the optical and X-ray data does not correspond to either the narrow or broad pulses (see Figure 5). We interpret this feature as a flare. If the flare were due to chromospheric activity from the M-dwarf, increased amplitude towards the ultraviolet would be expected[40,41]. That is not what we observe (see Extended Data Figure 5). Instead, we propose that this is an accretion-induced flare, suggestive of mass transfer and subsequent ejection between the M-dwarf and white dwarf (more details in the Methods section). This is in contrast to AR Sco, which shows no evidence whatsoever of ongoing accretion. Recent models for the evolution of magnetic white dwarfs in close binaries[17] predict accretion to cause the white dwarf spin-up, magnetic field generation, and subsequent detachment of the white dwarf from its companion. The flares in J1912−4410 suggest that **not enough energy has been transferred from spin to orbit to fully detach the system yet, which would suggest it is in a slightly** earlier stage of this formation scenario than AR Sco.

The discovery of J1912−4410 offers support for the rotation- and crystallisation-driven dynamo model as the origin of magnetic cataclysmic variables. It establishes binary white dwarf pulsars as a class, and provides evidence for residual accretion as predicted by the models[17]. **The M-dwarf companion is estimated to be nearly filling its Roche lobe, in agreement with the models and explaining any residual mass transfer. The upper limit on the white dwarf temperature is consistent with the onset of crystallisation, suggesting an emerging magnetic field that provides synchronising torque, which will fully detach the system once enough energy is transferred from the white dwarf spin to the orbit. The orbital period of the system is also in agreement with current model predictions.** Assuming AR Sco and J1912−4410 are the only two binary white dwarf pulsars in the thin disk suggests a space density of 0.15 ± 0.10 kpc^{-3}, taking into account the effective volume given by the thin disk stellar density[42]. This should be regarded as a lower limit, as ongoing searches might reveal other members of this class.

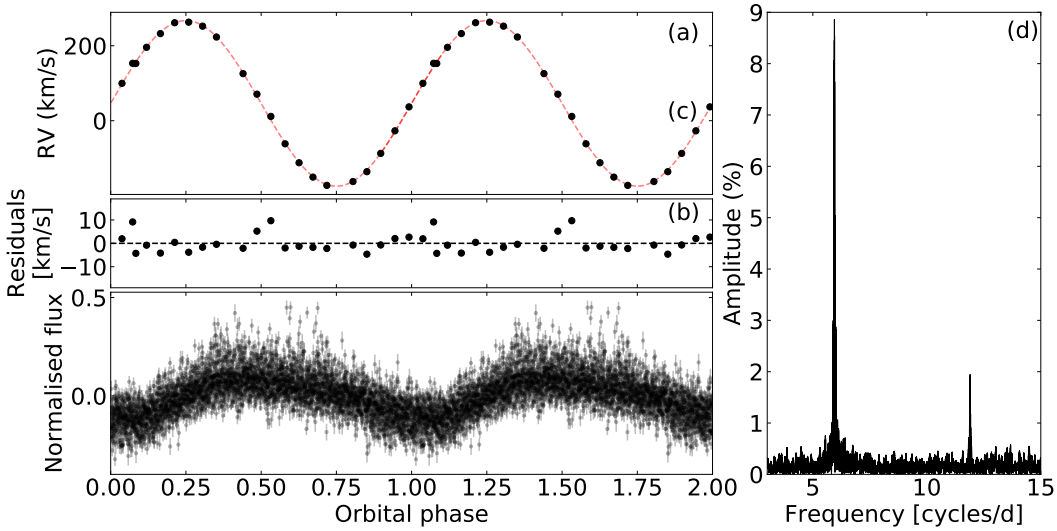

Figure 1. J1912−4410's photometry and radial velocities. Panel (a) shows the radial velocities obtained from the NaI doublet lines (8183 and 8195 Å) phased to the orbital ephemeris (Eq. 2). The red dashed line is a sinusoidal fit used to obtain the radial velocity semi-amplitude of the M-dwarf. Uncertainties are of the same order as the symbol size. Panel (b) shows the residuals when the sinusoidal is subtracted. Panel (c) shows the TESS data **with one-sigma uncertainties** folded on the orbital ephemeris. The Fourier transform of the TESS data is shown in panel (d), evidencing the orbital period (strongest peak) and its first harmonic.

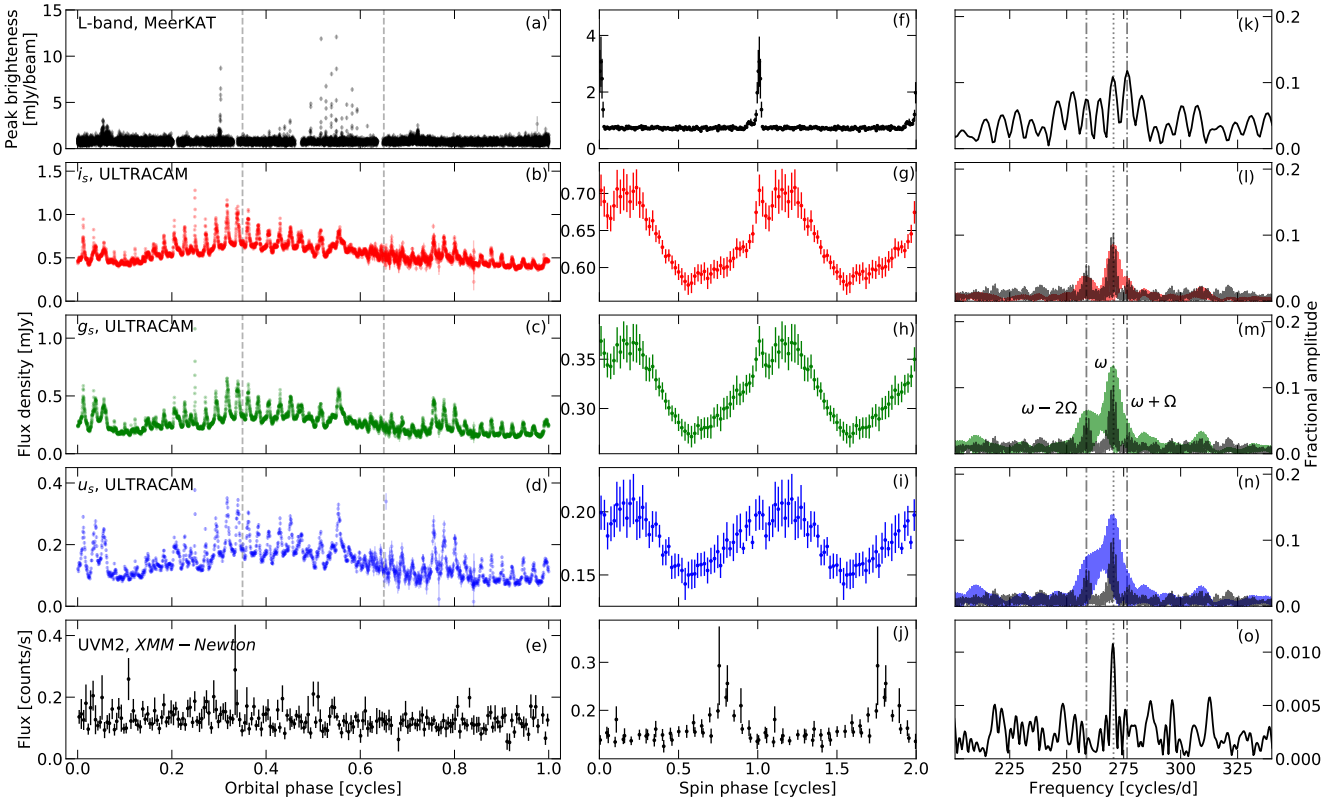

Figure 2. Radio, optical, and X-ray fluxes of J1912−4410. The panels on the left show high-speed photometry obtained with MeerKAT (a), with ULTRACAM (b–d, filters i_s, g_s, and u_s, respectively), and *XMM-Newton* (e) as a function of orbital phase. For *XMM-Newton*, the full dataset was phase-averaged, whereas for MeerKAT the data covering two orbits were folded with no averaging. For ULTRACAM, we show unfolded data for one orbit. **One-sigma error bars are shown in all panels, but are sometimes comparable to symbol size.** The dashed vertical lines mark regions of orbital phase that were selected for the spin-phase average pulses shown in the central panels, (f) to (j). For *XMM-Newton*, the whole dataset was used. **The error bars show the uncertainty on the mean in each phase bin.** The panels on the right show the Fourier transform for each dataset, with the main frequency combinations between spin (ω) and orbit (Ω) identified in panel (m). For MeerKAT we used only data around orbital phase 0.5, where the pulses are visible, to calculate the Fourier transform. For ULTRACAM, all data for the five nights are included. We also plot the Fourier transform of the HIPPO data, in which the peaks indicated by dashed lines are better resolved, in the background of panels l–n.

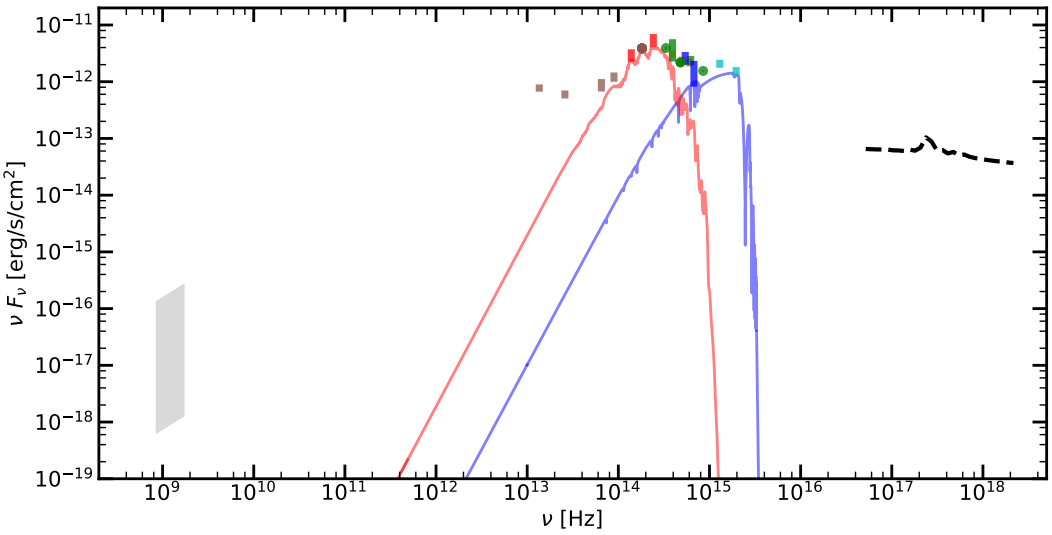

Figure 3. Spectral energy distribution of J1912−4410. The red and blue lines show model atmospheres assuming parameters close to the constraints that we placed for the M star ($R_2 = 0.3$ R$_\odot$, $T_2 = 3100$ K) and white dwarf (log $g = 9.0$**, and** $T_1 = 13000$ **K)** at the *Gaia* distance of 237 pc. The grey polygon shows the flux and frequency ranges observed in radio. The dashed line models the *XMM-Newton* spectrum in X-rays**, which combines a power law and absorption due to cold interstellar matter**. The coloured symbols show the other flux measurements, with vertical bars spanning minimum to maximum values when more than one measurement is available. From left to right, the flux values are W4, W3, W2, W1, H, J, K, z, i, r, V, g, U, u, NUV, and FUV.

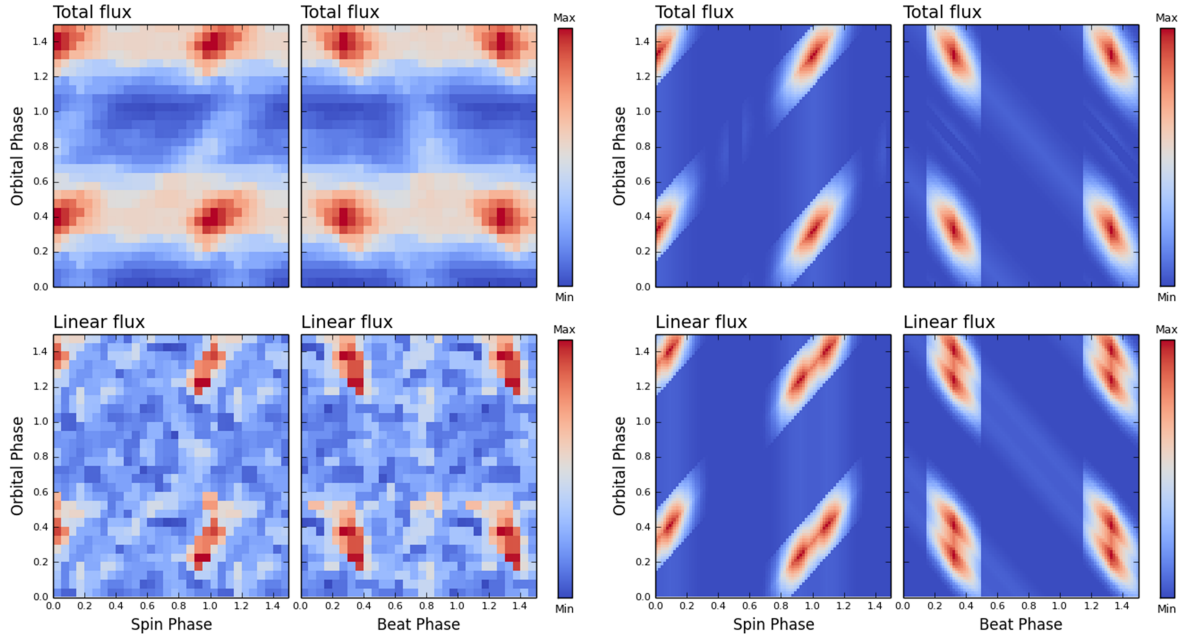

Figure 4. Photopolarimetry of J1912−4410. The four images on the left show the total intensity (upper two images) and linear polarisation (lower two images). The four images on the right show the model simulations of synchrotron emission from one emission region located close to one magnetic pole of a spinning white dwarf. The images show how the spin and beat (left and right columns, respectively) pulse profiles change with orbital phase. The images represent the averaged phase-folded data of all the photo-polarimetric observations. The total and linear flux have been normalised.

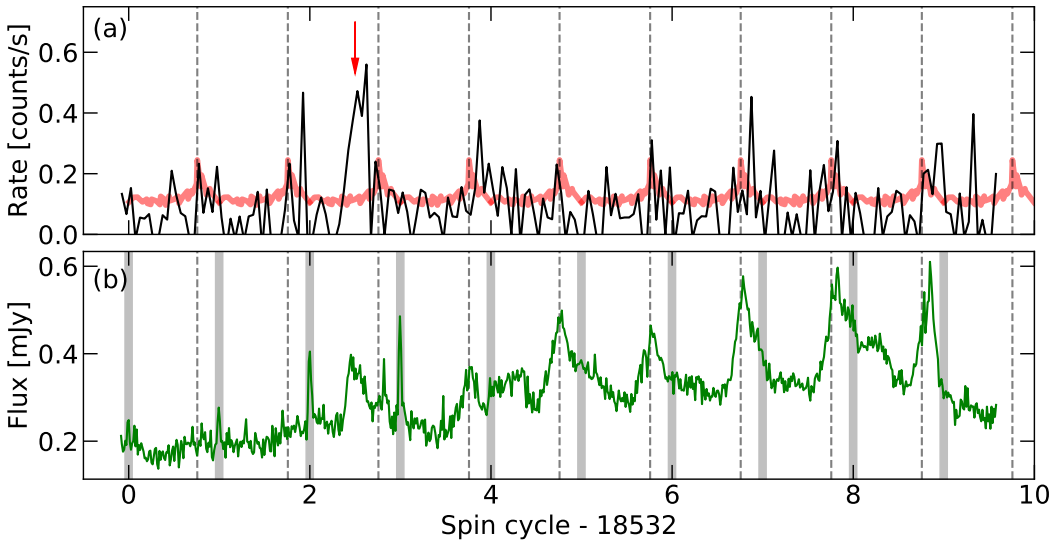

Figure 5. Simultaneous *XMM-Newton* and ULTRACAM data. Panel (a) shows in black the *XMM-Newton* data taken simultaneously with the ULTRACAM g_s data shown in panel (b). The red curve in panel (a) is the spin-phase average *XMM-Newton* data over the whole observation. The grey shaded areas in panel (b) indicate integer spin cycles, which coincide with the narrow pulses, whereas the dashed grey lines shown in both panels mark the maxima of the broad X-ray pulses. The red arrow indicates a feature that cannot be explained by either the narrow or the wide pulses, which we interpert as a flare.

Methods

Observations and data reduction

Time-series photometry: J1912−4410 was observed with ULTRACAM mounted on the 3.58 m ESO NTT on five nights. ULTRACAM uses dichroic beam splitters that allow simultaneous observations in three filters. We used so-called "super" SDSS filters, whose cut-on/off wavelengths match those of the commonly used Sloan Digital Sky Survey (SDSS) filters, but with a higher throughput[43]. For the first three nights, u_s, g_s, i_s filters were installed, and for the next two u_s, g_s, r_s filters were in place. We used the same exposure time for g_s, r_s, i_s filters, but set it to a factor of 3 or 4 times longer for u_s. Frame transfer capabilities were used so that the dead time between exposures was negligible. Supplementary Table 1 provides information about each of our runs. We performed bias subtraction and flat field correction, with skyflats taken during twilight, using the HiPERCAM data reduction pipeline[2]. The pipeline was also employed to carry out aperture photometry. We used a variable aperture size set to scale with the seeing estimated from a point-spread function (PSF) fit. The same constant comparison star, Gaia EDR3 6712712349514963072 ($G = 13.8$), was used in all runs. SkyMapper[44] data were used to calibrate the photometry to an approximate flux scale.

Supplementary Table 1. Log of ULTRACAM observations of J1912−4410.

Date	Start time (UT)	Duration (min)	Filter	Cadence (s)
2022-04-28	08 : 49 : 29	31	u_s	18.6
			g_s	6.2
			i_s	6.2
2022-06-07	02 : 02 : 02	276	u_s	32.0
			g_s	8.0
			i_s	8.0
2022-06-08	05 : 21 : 30	243	u_s	9.1
			g_s	3.0
			i_s	3.0
2022-09-18⋆	03 : 20 : 35	51	u_s	12.1
			g_s	4.0
			r_s	4.0
2022-09-24	00 : 30 : 08	237	u_s	8.5
			g_s	2.8
			r_s	2.8

⋆ Simultaneous with *XMM-Newton*.

Photopolarimetry: Photopolarimetry was performed with HIPPO[29] on the 1.9-m telescope of the South African Astronomical Observatory during the nights of 2022 June 29 and 30, 2022 July 3–5, as detailed in Supplementary Table 2. Observations

[2]https://github.com/HiPERCAM/hipercam

were through a clear filter (3500 − 9000 Å) defined by the response of the two RCA31034A GaAs photomultiplier tubes. Observations of polarised and non-polarised standard stars were made during the course of the observation run in order to calculate the waveplate position angle offsets, instrumental polarisation, and efficiency factors. The photometry is not absolutely calibrated and is instead given as total counts minus the background-sky counts. J1912−4410 was observed for a total of ~ 32 hours.

Supplementary Table 2. Log of HIPPO observations of J1912−4410. The cadence was 5.0 s for all runs.

Date	Start time (UT)	Duration (min)
2022-06-29	20:09:09	477.3
2022-06-30	20:27:09	460.8
2022-07-03	23:01:09	274.5
2022-07-04	19:53:34	252.1
2022-07-05	20:14:24	462.0

Spectroscopy: Two exploratory spectra to confirm J1912−4410's similarity with AR Sco were obtained with SOAR on 2022 August 28 during time obtained for project SO2022A-016. The data were reduced using `iraf`'s `noao` package. Upon confirmation of that J1912−4410's had spectral features like those seen in AR Sco, we obtained Director's Discretionary Time (DDT) with X-shooter (proposal 109.24EM) to cover one full orbital period. The observations were carried out on 2022 July 24, between 03:30:06 and 08:00:20 UT. We used a 1 arcsec slit for the UVB arm (300-559.5 nm, $R = 5400$), and 0.9 arcsec slits for the VIS (559.5-1024 nm, $R = 8900$) and NIR (1024-2480 nm, $R = 5600$) arms. The exposure time in the UVB arm was set to a fifth of the spin period (63.6 s) to sample the spin variability, and we obtained 168 exposures. In the VIS arm, the exposure was set to twice the spin period (636.4 s) to average out the effect of the spin variability, as our main interest with the VIS was to characterise the M-dwarf companion. 21 exposures were obtained. Finally, in the NIR arm the exposure was equal to the spin period (318.2 s) and we obtained 42 exposures. 2x2 binning was used to reduce the readout time, which was of 28 s in UVB, 34 s in VIS and 8.2 s in NIR. Automatic flexure compensation (AFC) exposures were obtained every 1.5 h. The X-shooter data were reduced using the `xsh_scired_slit_stare` routine in the ESO Recipe Execution Tool (EsoRex), and telluric line removal was performed with `molecfit`[45,46].

We also obtained medium-resolution (5.7Å) time resolved spectra over the wavelength range 4060–7120 Å of J1912−4410 on 2022 June 26 using the Robert Stobie Spectrograph (RSS)[47–49] on the Southern African Large Telescope (SALT)[50]. Two observations of 3000 s were obtained during both the rising (east) and setting (west) tracks, commencing respectively at 20:10:54 UTC and 02:37:53 UTC. Frame transfer mode was used, with 60 repeat 50 s exposures for each observation, with no dead-time.

The spectra were reduced using the `PySALT` package[51], which includes bias subtraction, flat-fielding, amplifier mosaicing, and a process to remove cosmetic defects. The spectra were wavelength calibrated, background subtracted, and extracted using standard IRAF[3] procedures. We obtained a relative flux calibration of all spectra using the spectrophotometric standard star Feige 110. The frame-transfer observations were used to create trailed spectra in order to investigate emission line variability.

X-rays: The original X-ray detection of J1912−4410 was made during eRASS1, the first X-ray all sky survey with *eROSITA* on the Spektrum-Roentgen-Gamma mission[28,52]. The eRASS1 proto-catalogue internal to the collaboration[4], which was produced with processing version c947[53], lists the detection of J1912−4410 at RA= 288.05807, DEC= −44.17913. Source detection was performed on an image using photons in the $0.2-2.3$ keV band. The source was found at a rate of 0.35 ± 0.07 s^{-1}, which corresponds to a flux of $(3.3\pm0.7)\times10^{-13}$ erg cm^{-2} s^{-1}.

Detailed follow-up was obtained with *XMM-Newton* following a DDT request. *XMM-Newton* observed the field of J1912−4410 on 2022 Septemper 17/18 for a total of 43 ks. For approximately 50 min, ULTRACAM observations were carried out simultaneously with *XMM-Newton*. The EPIC X-ray cameras were operated in full frame mode, and the optical monitor was used in fast imaging mode (time resolution 0.5 s) with the UVM2 filter (effective wavelength 231 nm). The original data were reduced with the latest version of the *XMM-Newton* SAS (SAS 20.0) using the most recent calibration files. Light curves and spectra were produced using the signal in concentric annuli around the source position to correct for background contamination. The mean rate in EPIC-pn was 0.0825 s^{-1} ($0.2-10$ keV).

The mean X-ray spectrum was analysed with XSPEC (version 12.12.0)[54]. An emission model as the sum of a power law (power law index 2.14 ± 0.11) and a thermal component ($kT=1.24\pm0.11$ keV) modified with absorption due to cold interstellar matter ($N_H=(5\pm2)\times10^{20}$ cm^{-2}) reflected the data satisfactorily. The best-fit model parameters yielded the model shown in Fig. 3. A full description of the X-ray data analysis including data from all *eROSITA* surveys and the *XMM-Newton* data will be presented separately (Schwope et al. 2023, in preparation).

Radio: An exploratory observation of J1912−4410 was made with MeerKAT's L-band receivers (856–1712 MHz) for one hour on 22 June 2022 (block ID 1655920939). Following the detection of pulses, a longer observation was made on 26 June 2022 (block ID 1656263834). The total on-target time was 7.55 hours, with the correlator configured to deliver 2 s integrations, which defines the minimum imaging timescale. Instrumental bandpass and delay corrections were derived from scans of the primary calibrator PKS B1934−638, and time dependent complex gains were derived from scans of the secondary calibrator J1830−3602. The `casa` package[55] was used for reference calibration and flagging of the calibrator scans. These gain corrections were then applied to the target field, which was flagged using the `tricolour` software[56]. The target data were imaged with `wsclean`[57], and self-calibrated using `cubical` `kenyon2018`. The data reduction scripts[58] that perform the processing up to this point are available online[5], and contain detailed lists of all the parameters used.

Following self-calibration and a final round of deconvolution, the resulting set of spectral clean components (excluding

[3]IRAF is distributed by the National Optical Astronomy Observatory, which is operated by the Association of Universities for Research in Astronomy (AURA) under cooperative agreement with the National Science Foundation (NSF).

[4]The full catalogue will be published by Merloni et al., in preparation.

[5]`oxkat`, v0.3, https://github.com/IanHeywood/oxkat

the position of J1912−4410 itself) were inverted into a set of model sky visibilities and subtracted from the data. This residual visibility set was then imaged using `wsclean`, producing an image for every 2 s timeslot in the observation (13,552 snapshot images in total). **We experimented with deriving an in-band spectral index using the strongest pulses, but found considerable scatter between pulses, with values ranging from -4.4 to -0.8 for different pulses and uncertainties reaching 40%. The median suggests a steep negative spectral index of ≈ -3, but higher signal-to-noise ratio than currently available is required to obtain robust and conclusive results.**

Archival data: J1912−4410 was observed by TESS during sectors 13 and 27, with a cadence of 30 min and 10 min, respectively. We downloaded postcards and performed aperture photometry using `eleanor` in a custom script[6]. We also downloaded photometry taken with the cyan (c) and orange (o) filters from the ATLAS archive[7]. Data were also available in CRTS and ASAS-SN, but due to the target's relative faintness we could not identify any of the periodic variability seen in other data in CRTS or ASAS-SN data, which we therefore employed no further.

The companion subtype and the orbital ephemeris

To determine the spectral subtype of the companion, we used the VIS arm of the X-shooter spectra. To minimise contribution from the white dwarf, both direct and due to its irradiation on the M-star, we started by deriving radial velocities for the Hα emission line by fitting it with a Gaussian profile. Hα should trace the irradiated face of the companion (as later confirmed, see the section "Doppler tomography and the origin of emission"), hence by fitting the velocities with a sinusoidal we were able to estimate the point at which the companion is at its closest approach to Earth, when contribution from the white dwarf is minimised. The spectrum closest to inferior conjunction was then employed for spectral subtype determination. We fitted the observed spectrum using M-dwarf templates obtained with the same X-shooter configuration[59] as our observations. The template fluxes were scaled by a factor α and combined with a smooth continuum to account from any extra flux in addition to the M-star. This was parameterised by $\exp(a_1 + a_2\lambda)$ to ensure positivity[3]. To focus on the M-dwarf contribution as well as avoid noisy regions, we only fit the spectrum between 6800 and 9250 Å. Additionally, we masked the CaII emission triplet lines around 8500 Å. Similar values of χ^2 were obtained for the M4, M4.5, and M5 templates, hence we concluded the companion to be of type M4.5 $\pm$ 0.5.

Once the spectral type was determined, we proceeded to estimate the radial velocity of the M-dwarf by cross-correlating the NaI 8200 Å doublet absorption lines, which should more closely trace the centre of mass than the emission lines, with a spectral template. We found the M4.0 template to provide a better fit in this region, and therefore used it in the cross-correlation. We normalised the region within 8140–8240 Å by the continuum using a first order polynomial, and then subtracted a first-order spline fit to the normalised continuum. The same procedure was applied to the 21 VIS spectra and the template, which were then binned to the same velocity scale and cross-correlated. The obtained radial velocities are listed in Supplementary Table 3.

To determine the orbital ephemeris, the obtained radial velocities were combined with an orbital period measurement from TESS data, whose time span and continuous coverage is ideal for precisely determining the orbital frequency. The Fourier

[6]https://github.com/ipelisoli/eleanor-LS
[7]https://fallingstar-data.com/forcedphot/

Supplementary Table 3. Radial velocities obtained for J1912−4410. Radial velocities and one-sigma uncertainties obtained for the M-dwarf in J1912−4410 using the NaI 8200 Å doublet absorption lines.

BJD(TDB)	RV (km/s)	σ_{RV} (km/s)
2459784.65911	153.2	3.6
2459784.66687	195.8	3.5
2459784.67463	232.4	3.6
2459784.68259	261.5	4.0
2459784.69042	262.9	4.1
2459784.69818	252.2	4.5
2459784.70593	223.3	4.4
2459784.72079	125.6	5.0
2459784.72855	70.8	4.6
2459784.73632	11.4	4.6
2459784.74427	-61.7	4.6
2459784.75208	-112.2	4.5
2459784.75984	-150.5	3.9
2459784.76760	-172.5	4.0
2459784.78221	-162.3	3.9
2459784.78997	-136.0	4.7
2459784.79771	-87.2	5.0
2459784.80566	-27.0	5.2
2459784.81350	36.8	4.8
2459784.82127	99.7	4.4
2459784.82901	152.7	4.8

transform of the TESS data showed a strong peak near 5.95 cycles/d, with the first harmonic also clearly visible (see Fig. 1). We interpreted this as the orbital frequency, which is in agreement with the observed radial velocity variability **and within the orbital period range predicted for white dwarf pulsars[17].**

Reflection alone cannot explain the observed photometric orbital modulation, which is asymmetric and shows amplitude higher than the sub-percent that would be expected for a reflection effect for the system's estimated parameters at low inclination (which we find to be the case for J1912−4410, as discussed in the next section). The larger amplitude can be explained by contribution from non-thermal emission when the rotational energy of the white dwarf is dissipated by interaction of its magnetic field with the M dwarf's. The asymmetry, also observed in AR Sco, has two proposed explanations[4]. The first is that the power dissipated by interaction between the star's magnetic fields is greater on the leading face of the M-dwarf, where shock occurs, than on its trailing face. The other possibility is that the spin axis of the white dwarf is misaligned with the orbit, which would cause the dissipation rate in the M dwarf to vary with orbital phase. A consequence of the latter is that precession of the spin axis would make the orbital phase of the maximum to drift, which has not been observed for AR Sco[60], but cannot be ruled out given that the precession period can be of up to several hundreds of years.

The system's orbital period and its uncertainty were determined via bootstrapping, using a Fourier model with two sine terms (one on the fundamental frequency, and one on the first harmonic) to fit the TESS data. We obtained $P_{\rm orb} = 0.16811989(36)$ days, corresponding to $\Omega = 5.948136(13)$ cycles/d. To determine the reference epoch (phase 0) of the ephemeris, defined here as the

inferior conjunction of the M-dwarf, we fitted the radial velocities with

$$V_R = \gamma + K_2 \sin[2\pi(t - T_0)/\Omega], \quad (1)$$

where γ is the systemic velocity, K_2 the radial velocity semi-amplitude of the M-dwarf, t the mid-exposure times of each spectrum yielding a measurement, T_0 the reference time of inferior conjunction, and Ω is the orbital period, which was fixed at the value obtained from the TESS data. Using bootstrapping to determine uncertainties, we obtained $\gamma = 46.2 \pm 1.0$ km/s, $K_2 = 220.9 \pm 1.1$ km/s, and $T_0 = 2459784.98308(19)$, thus the orbital ephemeris of J1912−4410 is:

$$BJD(TDB) = 2459784.98308(19) + 0.16811989(36)E, \quad (2)$$

where E is an integral cycle number, and BJD is the barycentric Julian date (in TDB scale).

Constraining the stellar masses

From the value of K_2 and the orbital period, we can use Kepler's third law to calculate the mass function:

$$f_M = \frac{M_1^3 \sin^3 i}{(M_1 + M_2)^2} = \frac{\Omega K_2^3}{2\pi G} = (0.1879 \pm 0.0027)\, M_\odot. \quad (3)$$

This equation, in which i is the orbital inclination, sets a lower limit to the mass of the unseen compact object, met for $M_2 = 0$ and $i = 90°$. This only stands if our assumption that the obtained radial velocities indeed trace the centre of mass of the M-dwarf is correct. As we detected no systematic deviation from a sinusoidal in the residuals (see Fig. 1), as would be expected if irradiation caused weakening of the absorption lines on the side of the cool star facing the compact companion, our assumption seems to be correct.

An independent constraint on the system's masses can be obtained from the difference between the semi-amplitudes derived from the emission lines (tracing the irradiated face) compared to the absorption lines (tracing the centre of mass), shown in Supplementary Table 4. The simple assumption that all measurements have to be within the M-dwarf's Roche-lobe results in $q > 0.1$, as illustrated in panel (a) of Extended Data Fig. 2. Requiring that star 1 is a white dwarf can provide a tighter constraint. Given the spin period of 5.3 min, too long for a neutron star but completely consistent with white dwarfs in magnetic cataclysmic variables[61], we consider this to be a fair assumption. As shown in panel (b) of Extended Data Fig. 2, this results in $q > 0.3$. This can be combined with Equation 3 to obtain a tighter constraint on M_1. Equation 3 implies

$$M_1 = f_M (1 + q)^2 / \sin^3 i. \quad (4)$$

Given the lower limit for q and upper limit for $\sin^3 i$ at $i = 90°$, we obtain $M_1 > 0.32$ M$_\odot$ and $M_2 > 0.095$ M$_\odot$.

We can also obtain an upper limit on the M-dwarf mass. For a Roche-lobe filling star, there is a tight relationship between

Supplementary Table 4. Radial velocity semi-amplitudes for different lines

Line	Semi-amplitude (km/s)
Hα	177 ± 5
Hβ	155.5 ± 1.1
Hγ	157.7 ± 1.0
NaI doublet	220.9 ± 1.1

orbital period and mean density ρ[37]:

$$\rho[\mathrm{g/cm^3}] \quad = \quad (0.43/\Omega[\mathrm{days}])^2. \tag{5}$$

Because the mean density of a main-sequence star decreases with increasing mass, this corresponds to an upper limit. Assuming a semi-empirical mass-radius relationship[62], which takes the M-dwarf inflation problem[63] into account, results in $M_2 < 0.42$ M$_\odot$. Combining the limit given by the M-dwarf filling its Roche lobe with the observed K_2 values also implies a maximum inclination at which star 1 is a white dwarf. Higher inclinations would require a more compact M-dwarf to explain the observed K_2 difference, which in turn requires the compact object to have a higher-mass so that the M-dwarf still fills the Roche lobe. The maximum system inclination is $i < 37°$, as demonstrated in Extended Data Fig. 2.

Equation 4 can also be interpreted as a relationship between M_1, M_2, and inclination. With the limits derived above, useful constraints can be obtained. This is shown in Extended Data Figure 3. The upper limit on inclination requires the white dwarf mass to be above ≈ 1.0 M$_\odot$. To further constrain the masses, we can rely on an estimate for M_2 obtained from an estimate of the stellar radius. The distance to J1912−4410 is well constrained by the *Gaia* parallax to $d = 237 \pm 5$ pc. Hence, when fitting the observed spectrum to models, the **previously mentioned** scaling factor α, which corresponds to $(R_2/d)^2$, provides a radius estimate. Combining this with a mass-radius relationship gives M_2. We fitted NextGen models[64] to the M-dwarf spectra via χ^2 minimisation using the same wavelength region as employed to obtain the M-dwarf subtype. We kept the log g fixed at 5.5 rather than free, given that the effects of gravity and rotation on the line widths cannot easily be disentangled. We obtained $T_2 = 3\,100 \pm 100$ K and $R_2 = 0.23 \pm 0.02$ R$_\odot$. Using the same mass-radius relationship as above results in $M_2 = 0.26 \pm 0.02$ M$_\odot$. The quoted uncertainties are statistical only. For R_2 and M_2, the M-dwarf inflation problem suggests that the uncertainty is of the order of 15%. The irradiation of the M-dwarf by the white dwarf, which can also cause inflation, leads to similar uncertainty[65]. The derived M_2 value implies a white dwarf mass of ≈ 1.2 M$_\odot$. To take into account the large systematic uncertainties in M_2, we adopt the mass values of $M_1 = 1.2 \pm 0.2$ M$_\odot$ and $M_2 = 0.25 \pm 0.05$ M$_\odot$ quoted in the main text. **These masses imply $q \sim 0.21$, and hence a Roche-lobe radius of ~ 0.25 R$_\odot$[37] for the M-dwarf, close to our estimated radius, suggesting that the M-dwarf is near Roche-lobe filling, as inferred for AR Sco[38] and as predicted for a white dwarf pulsar configuration[17].**

The spin and beat frequencies

The ground-based fast photometry obtained with ULTRACAM and HIPPO was used to determine the spin frequency of J1912−4410. This identification is not as straightforward as the orbital period. Fourier transform of the ULTRACAM and HIPPO data showed three main peaks separated by multiples of the orbital frequency. We also analysed light curves derived from the continua and emission lines of observed spectra (see Supplementary Figure 1), which show in turn only one resolved peak. The lines originate in the irradiated face of the companion, hence their variability would likely reflect the reprocessed or beat frequency. The resolution of the spectral Fourier transforms is, however, not high enough to separate spin and beat frequencies. We ultimately relied on the modelling of the photopolarimetry (see Section "Photopolarimetry and modelling of the emission") to determine whether the dominant frequency is the spin or beat, concluding that the data can be better explained by the models if the former is the dominant frequency. Therefore we interpret the two main peaks as ω and $\omega - 2\Omega$, with $\omega + \Omega$ also being marginally detected. The absence of the beat frequency is somewhat puzzling, although $2(\omega - \Omega)$ is detected (Supplementary Figure 2). This could be a consequence of low inclination, such that reprocessed radiation from only one pole is detected.

To determine the spin ephemeris, we measured pulse arrival times from both the HIPPO and the ULTRACAM data. We first estimated ω and the time of maxima T_0^{ω} values by fitting a cosine function to the ULTRACAM g_s data, after subtracting the orbital modulation. This trial ephemeris was used to estimate the approximate pulse arrival times and cycle numbers expected from each dataset. To refine this estimate, we cross-correlated the data around each expected peak with a Gaussian function, and found the time of maxima by locating the maxima of the cross-correlation function using the Newton-Raphson method.

This procedure of estimating times of maxima given trial ephemeris and subsequently fitting the obtained values was repeated until the trial and fitted ephemeris showed no significant change. The σ width of the Gaussian was fixed at a value of 15 s, which we found to yield a good balance between identified pulses and fit residuals (i.e. a large number of pulses was obtained, and the identifications were good enough that the residuals to the fit were not increased. Increasing the value of σ resulted in lower residuals, but fewer identified pulses, whereas decreasing the value increased the number of identified pulses, but also increased residuals).

Next we fitted the obtained cycle numbers and time of maxima assuming linear ephemeris. The residuals of the fit are modulated with orbital phase, as illustrated in Supplementary Figure 3. The semi-amplitude of the modulation is of the order of 15 s, significantly in excess of the $\lesssim 1.5$ s that could be explained by the difference in light travel time throughout the orbit. This behaviour likely arises due to the varying contribution of beat, spin and their harmonics to the pulse shape throughout the orbit, as seen in AR Sco[38,66,67], and suggests that the line-of-sight geometry plays a role in the detected emission. To minimise the effect of this in the ephemeris determination, we fitted the orbital modulation with a Fourier series (one sine and cosine component) and subtracted the modulation from the derived times. We additionally excluded from the fit any measurements with a residual larger than 0.25 cycles.

We initially fitted each dataset (HIPPO and each of the ULTRACAM filters) independently to probe for dependence of the

pulse arrival times with wavelength (as seen for AR Sco[38,67]). We found the ephemeris to be consistent between datasets, and hence fitted all data together. Following the described procedure, we obtained the following spin ephemeris:

$$BJD(TDB) = 2459772.142522(24) + 0.0036961693(10)E, \quad (6)$$

where E is an integral cycle number. The best fit and uncertainties were determined via bootstrapping.

Additionally, we have probed for the occurrence of spin-up or spin-down, as observed for AR Sco[3,38,66,67], by fitting a quadratic ephemeris and performing an F-test to determine whether the addition of a quadratic term significantly improved the fit. We have found that for none of the our datasets a quadratic fit represented a significant improvement, which is unsurprising given our short baseline. We attempted to increase our baseline by deriving a pulse arrival measurement from the ATLAS c data, which shows a hint of the spin period in its Fourier transform. Our approach was to subtract the orbital modulation modelled by a Fourier series, and fit the residuals with a cosine with period fixed to the spin period, but we found that the large uncertainties resulted in a poor fit with an amplitude consistent with zero. Therefore, a constraint on the spin period change could not be obtained with the current data.

The possible occurrence of flares

The optical observations of J1912−4410 often showed hints of flaring, with the amplitude of the possible flares even dominating over the orbital modulation in a few occasions (see Supplementary Figure 4). We studied the possibility of flares in more detail using the simultaneous *XMM-Newton* and ULTRACAM data, as shown in Figure 5. The simultaneous data covers orbital phases 0.05 to 0.26, where typically the optical pulses are weak and less sharp. Yet, several narrow features consistent with the location of spin maxima are seen (in particular at spin cycles 18532–18535). The X-ray pulses, in contrast, are displaced in phase compared to narrow pulses, but coincide with wider features in the optical data. Our interpretation is that the short-lived features seen in the ULTRACAM data originate in the magnetosphere of the white dwarf, thus repeating on the spin period. As seen in Fig. 2, they are associated with the narrow pulses seen in radio data. The broader features seen in both ULTRACAM and *XMM-Newton* show an offset compared to the narrow maxima (as also seen in Fig. 2), suggesting they originate in another region in the system, possibly near the M-dwarf companion where the strongest emission is observed.

Associating the narrow features with the magnetosphere of white dwarf and the broader pulses with emission elsewhere, causing a phase delay, still leaves at least one unidentified feature around cycle 18534.5. The amplitude of this feature shows no apparent colour dependency (Extended Data Figure 5), unlike M-dwarf flares. We suggest that these are flares induced by accretion along the white dwarf's magnetic field lines. If this interpretation is correct, it would imply that, unlike AR Sco, J1912−4410 is not completely detached yet, thus being in an earlier stage of evolution according to the model of Schreiber et al. 2021[17]. Continuous monitoring of this source to probe the occurrence of flares will allow testing this hypothesis.

Constraining the white dwarf temperature

The temperature of the white dwarf is a crucial parameter, especially in the context of the theoretical model proposed to explain the origin of binary white dwarf pulsars[17]. In this model, the generation of the white dwarf magnetic field, which eventually becomes strong enough to connect with the M-dwarf magnetic field and provide a synchronising torque that explains the fast spin-down of systems like AR Sco, has been attributed to crystallisation- and rotation-driven dynamo. Therefore, the white dwarf must have cooled down enough for crystallisation to progress in the core. For the range of masses derived, crystallisation will start below temperatures of $35\,000 - 14\,000$ K for a carbon-oxygen core white dwarf, depending both on the white dwarf mass and on the thickness of its atmosphere[68].

To constrain the white dwarf temperature, we analysed the X-shooter UVB spectra taken near the minimum flux (orbital phase 0.95 to 1.05). The spectra were co-added and compared to white dwarf models[69] with $\log\ g = 8.5$ **or** $\log\ g = 9.0$ (consistent with our estimated mass range) and a range of effective temperatures. Models were scaled taking into account J1912−4410's distance and a white dwarf radius interpolated from cooling models for each temperature[68,70]**, assuming a mass of 1.0 $M_\odot$ for** $\log\ g = 8.5$ **and 1.2 $M_\odot$ for** $\log\ g = 9.0$**. We assumed carbon-oxygen cores in both cases, although a oxygen-neon-magnesium composition might be more likely for a mass of 1.2 $M_\odot$[71].** Our approach is illustrated in Supplementary Figure 5 **for the 1.0 $M_\odot$ case**. The flux itself places only a loose constraint, as shown in panel (a): requiring that the model flux does not exceed the observed flux suggests $T_1 \lesssim 26\,000$ K. A tighter constraint can be obtained from the shape of the emission lines, as illustrated in panel (b). Our approach was to subtract the scaled white dwarf model from the observed spectrum and identify when that introduced a slope near the emission lines, suggesting that the white dwarf absorption line should be visible at that temperature, which is not the case for the observed spectrum. To numerically determine when there is a significant slope, we fitted the continuum near the Hγ line, where the spectrum is close to flat, after subtracting the scaled model. We fit both using a constant and a first order polynomial (indicating a slope), and perform an F-test to determine when the slope becomes significant. This suggested $T_1 < 13\,000$ K, above which the wings of the absorption lines of the white dwarf would be detectable. **For a mass of 1.2 $M_\odot$, the upper limit becomes 23 000 K. However, in this case, the GALEX FUV flux would be higher than observed. The FUV flux places an upper limit of $T_1 < 18\,000$ K for 1.2 $M_\odot$, with extinction at J1912−4410's distance and sky direction taken into account[72]. For 1.2 $M_\odot$, crystallisation starts around 20 000 K for a carbon-oxygen core[68], and around 24 000 K for a oxygen-neon core[73], therefore the upper limit would imply crystallisation already started. The 1.0 $M_\odot$ case is less conclusive: the upper limit of $T_1 < 13\,000$ K is consistent with the FUV (see Fig. 3), and crystallisation starts just around this temperature[68]. Hence our upper limit cannot rule out that the core is not significantly crystallised, but is consistent with it being at least starting to crystallise. Since the 1.0 $M_\odot$ case is the less conclusive in terms of crystallisation, it is the one we have focused on and illustrated in the main text.**

Doppler tomography and the origin of emission

The X-shooter spectra cover a full orbital period, allowing us to employ the Doppler tomography technique[74], which maps the observed line profiles at different orbital phases into velocity space. This allows the emission distribution in the binary to

be mapped. We computed Doppler maps for Hβ, Hα, and the CaII triplet around 8500 Å. The trailed line profiles for these lines can be seen in Supplementary Figure 6. For Hα (panel b), in additional to the sinusoidal profile due to orbital motion, satellite lines extending to higher velocities can be seen, similarly to what has been observed for AR Sco[75]. Frame-transfer spectroscopy also showed that Hα is seen to pulsate with a period closer to the spin period (see Supplementary Figure 7). Corresponding Doppler maps are shown in Supplementary Figure 8. It can be seen that the emission originates mainly at the irradiated face of the M-dwarf, with a somewhat extended region towards the white dwarf for Hα and Hβ. Hα additionally shows signs of prominences around -200 and 200 km/s, a pattern also seen in the Doppler maps of AR Sco[38,75]. Though these prominences could be attributed to accumulated material in these regions, possibly due to the magnetic field altering the Roche geometry and placing stable Lagrange points at these locations[76], an alternative is that the Hα line profile has components that are not kinematic in origin, but result from variations in optical depth or other changes in the radiative transfer in the M-dwarf photosphere that change the line profile independently of velocity. This suggestion is motivated by the fact that Hα is seen to show atypical line profiles even in some detached binaries of M-dwarfs with white dwarf companions[77].

Photopolarimetry and modelling of the emission

An example of a single night's (29 June 2022) time-series photo-polarimetry data is shown in Supplementary Figure 9. The orbital modulation and the short period pulses are clearly seen in the photometry. The circular polarisation appears consistent with zero percent. The linear polarisation averages around 4 percent, although some single data points show larger values, up to 12 percent (see Supplementary Figure 10, which zooms into the region where the linear polarisation pulses can be seen). The linear polarisation data is of insufficient signal-to-noise to be binned with enough time resolution to show the photometric pulses. Therefore, we subjected the entire series of photo-polarimetry to a Fourier analysis, for which the amplitude spectrum is presented in Supplementary Figure 11. The amplitude spectra, for both the photometry and the linearly polarised flux, display the most prominent peaks at the orbital frequency (Ω), the spin frequency (ω) and twice the beat frequency ($2(\omega-\Omega)$). There were no significant frequencies in the amplitude spectrum of the circular polarisation.

To increase the signal-to-noise, we phase-binned and folded the data on the spin and beat frequencies as a function of orbital phase (Figure 4, left-hand panels). These so-called dynamic pulse profiles show how the beat and spin variations are modulated on the orbital period. Immediately obvious is that both the photometric and linear pulses (spin and beat) evolve in amplitude over the orbital cycle, peaking at ~ 0.4 in orbital phase. The spin and beat pulses have a diagonal structure as they appear to drift later and earlier, respectively, as a function of orbital phase, thus indicating that the polarised emission has both spin and beat components. In addition, there is a fainter photometric pulse during orbital phases $\sim 0.6-1.1$. We performed the same exercise assuming the dominant frequency to be that of the beat, rather than the spin, which resulted in smeared features (see Supplementary Figure 12). **This significant increase in smearing when the beat is assumed to be dominant** indicates that the data have not been folded on the correct spin and beat frequencies. This was our main motivation behind the interpretation of spin as the dominant frequency. **In addition, the position angle of linear polarisation seems to be better defined when assuming the dominant peak to be the spin, though this is marginal at the moment and will require further follow-up to**

be confirmed (see Supplementary Figure 13).

The observed dynamic pulse profile is remarkably identical (in morphology and orbital phasing) to the main pulse in AR Sco (see fig. 2 of Potter & Buckley 2018[6]). On closer inspection, there may be an indication that the linearly polarised spin and beat pulses are diagonally split, in the same manner as the main pulse in AR Sco**, given that there seems to be a valley of lower intensity between peaks of higher intensity at each end of the profile. Future observations with higher signal-to-noise ratio will confirm whether this is a real feature**.

Given the observed photopolarimetric similarities between J1912−4410 and AR Sco, we adapted the simple synchrotron model previously used in the literature to explain AR Sco's emission[6]. The model photopolarimetric emission is shown as dynamic pulse profiles in the right-hand panels of Figure 4. The model assumes a synchrotron emission source is locked in the white dwarf rotating frame, which receives a further injection of electrons as the white dwarf's magnetic field sweeps past the secondary star on the beat frequency. The magnetic field of the rotating white dwarf accelerates the electrons to relativistic speeds, resulting in beamed synchrotron emission. We used the AR Sco model, but with a smaller inclination of 37° and with a single emission region instead of two. As can be seen from the right-hand panels of Figure 4, the model visually reproduces the observed dynamic pulse profile quite well, in particular the orbital phasing of the pulses and their morphology. The absence of a second emission region and a less significant splitting of the linear pulses in J1912−4410 compared to AR Sco is simply explained as an inclination effect, i.e. J1912−4410 is a lower inclination version of AR Sco.

Data availability

The TESS data used in this work are public and can be accessed via the Barbara A. Mikulski Archive for Space Telescopes (https://mast.stsci.edu/). Other data will be become public after the proprietary time expires, but can be made available upon reasonable request to the corresponding author.

Code availability

Any of the custom data analysis scripts used in this work can be made available upon reasonable request to the corresponding author.

References

1. Stanway, E. R. et al. VLA radio observations of AR Scorpii. *Astron. Astrophys.* **611**, A66 (2018).
2. Takata, J. et al. A Non-thermal Pulsed X-Ray Emission of AR Scorpii. *Astrophys. J.* **853**, 106 (2018).
3. Marsh, T. R. et al. A radio-pulsing white dwarf binary star. *Nature* **537**, 374–377 (2016).
4. Katz, J. I. AR Sco: A Precessing White Dwarf Synchronar? *Astrophys. J.* **835**, 150 (2017).
5. Takata, J., Yang, H. & Cheng, K. S. A Model for AR Scorpii: Emission from Relativistic Electrons Trapped by Closed Magnetic Field Lines of Magnetic White Dwarfs. *Astrophys. J.* **851**, 143 (2017).

6. Potter, S. B. & Buckley, D. A. H. Time series photopolarimetry and modelling of the white dwarf pulsar in AR Scorpii. *Mon. Not. R. Astron. Soc.* **481**, 2384–2392 (2018).

7. du Plessis, L. et al. Probing the non-thermal emission geometry of AR Sco via optical phase-resolved polarimetry. *Mon. Not. R. Astron. Soc.* **510**, 2998–3010 (2022).

8. Geng, J.-J., Zhang, B. & Huang, Y.-F. A Model of White Dwarf Pulsar AR Scorpii. *Astrophys. J. Lett.* **831**, L10 (2016).

9. Barnes, S. A. Ages for Illustrative Field Stars Using Gyrochronology: Viability, Limitations, and Errors. *Astrophys. J.* **669**, 1167–1189 (2007).

10. Hermes, J. J. et al. White Dwarf Rotation as a Function of Mass and a Dichotomy of Mode Line Widths: Kepler Observations of 27 Pulsating DA White Dwarfs through K2 Campaign 8. *Astrophys. J. Suppl. Ser.* **232**, 23 (2017).

11. Córsico, A. H., Althaus, L. G., Miller Bertolami, M. M. & Kepler, S. O. Pulsating white dwarfs: new insights. *Astron. Astrophys. Rev.* **27**, 7 (2019).

12. Patterson, J. The DQ Herculis Stars. *Publ. Astron. Soc. Pac.* **106**, 209 (1994).

13. Lyutikov, M. et al. Magnetospheric interaction in white dwarf binaries AR Sco and AE Aqr. *arXiv e-prints* arXiv:2004.11474 (2020).

14. Ghosh, P. & Lamb, F. K. Accretion by rotating magnetic neutron stars. II. Radial and vertical structure of the transition zone in disk accretion. *Astrophys. J.* **232**, 259–276 (1979).

15. Pala, A. F. et al. Constraining the evolution of cataclysmic variables via the masses and accretion rates of their underlying white dwarfs. *Mon. Not. R. Astron. Soc.* **510**, 6110–6132 (2022).

16. Wynn, G. A. & King, A. R. Diamagnetic accretion in intermediate polars - I. Blob orbits and spin evolution. *Mon. Not. R. Astron. Soc.* **275**, 9–21 (1995).

17. Schreiber, M. R., Belloni, D., Gänsicke, B. T., Parsons, S. G. & Zorotovic, M. The origin and evolution of magnetic white dwarfs in close binary stars. *Nat. Astron.* **5**, 648–654 (2021).

18. Isern, J., García-Berro, E., Külebi, B. & Lorén-Aguilar, P. A Common Origin of Magnetism from Planets to White Dwarfs. *Astrophys. J. Lett.* **836**, L28 (2017).

19. Ginzburg, S., Fuller, J., Kawka, A. & Caiazzo, I. Slow convection and fast rotation in crystallization-driven white dwarf dynamos. *Mon. Not. R. Astron. Soc.* **514**, 4111–4119 (2022).

20. Liebert, J., Ferrario, L., Wickramasinghe, D. T. & Smith, P. S. Enigmas from the Sloan Digital Sky Survey DR7 Kleinman White Dwarf Catalog. *Astrophys. J.* **804**, 93 (2015).

21. Parsons, S. G. et al. Magnetic white dwarfs in post-common-envelope binaries. *Mon. Not. R. Astron. Soc.* **502**, 4305–4327 (2021).

22. Pala, A. F. et al. A Volume-limited Sample of Cataclysmic Variables from Gaia DR2: Space Density and Population Properties. *Mon. Not. R. Astron. Soc.* **494**, 3799–3827 (2020).

23. Kato, T. & Kojiguchi, N. ZTF J185139.81+171430.3 = ZTF18abnbzvx: the second white dwarf pulsar? *arXiv e-prints* arXiv:2107.09913 (2021).

24. Kato, T., Hambsch, F.-J., Pavlenko, E. P. & Sosnovskij, A. A. Orbital and spin periods of the candidate white dwarf pulsar ASASSN-V J205543.90+240033.5. *arXiv e-prints* arXiv:2109.03979 (2021).

25. Kato, T. Gaia22ayj: outburst from a deeply eclipsing 9.36-min binary? *arXiv e-prints* arXiv:2203.13975 (2022).

26. Pelisoli, I. et al. A targeted search for binary white dwarf pulsars using *Gaia* and WISE. *In prep.* (2023).

27. Dhillon, V. S. et al. ULTRACAM: an ultrafast, triple-beam CCD camera for high-speed astrophysics. *Mon. Not. R. Astron. Soc.* **378**, 825–840 (2007).

28. Predehl, P. et al. The eROSITA X-ray telescope on SRG. *Astron. Astrophys.* **647**, A1 (2021).

29. Potter, S. B. et al. Polarized QPOs from the INTEGRAL polar IGRJ14536-5522 (=Swift J1453.4-5524). *MNRAS* **402**, 1161–1170 (2010).

30. Ricker, G. R. et al. Transiting Exoplanet Survey Satellite (TESS). *J. Astron. Telesc. Instruments, Syst.* **1**, 014003 (2015).

31. Tonry, J. L. et al. ATLAS: A High-cadence All-sky Survey System. *Publ. Astron. Soc. Pac.* **130**, 064505 (2018).

32. Drake, A. J. et al. The Catalina Real-time Transient Survey. In Griffin, E., Hanisch, R. & Seaman, R. (eds.) New Horizons in Time Domain Astronomy, vol. 285, 306–308 (2012).

33. Shappee, B. et al. All Sky Automated Survey for SuperNovae (ASAS-SN or "Assassin"). In American Astronomical Society Meeting Abstracts #223, vol. 223 of American Astronomical Society Meeting Abstracts, 236.03 (2014).

34. Clemens, J. C., Crain, J. A. & Anderson, R. The Goodman spectrograph. In Moorwood, A. F. M. & Iye, M. (eds.) Ground-based Instrumentation for Astronomy, vol. 5492 of Society of Photo-Optical Instrumentation Engineers (SPIE) Conference Series, 331–340 (2004).

35. Vernet, J. et al. X-shooter, the new wide band intermediate resolution spectrograph at the ESO Very Large Telescope. *Astron. Astrophys.* **536**, A105 (2011).

36. Caleb, M. et al. Discovery of a radio-emitting neutron star with an ultra-long spin period of 76 s. *Nat. Astron.* **6**, 828–836 (2022).

37. Eggleton, P. P. Aproximations to the radii of Roche lobes. *Astrophys. J.* **268**, 368–369 (1983).

38. Pelisoli, I. et al. Long-term photometric monitoring and spectroscopy of the white dwarf pulsar AR Scorpii. *Mon. Not. R. Astron. Soc.* **516**, 5052–5066 (2022).

39. Bailer-Jones, C. A. L., Rybizki, J., Fouesneau, M., Demleitner, M. & Andrae, R. Estimating Distances from Parallaxes. V. Geometric and Photogeometric Distances to 1.47 Billion Stars in Gaia Early Data Release 3. *Astron. J.* **161**, 147 (2021).

551 **40.** Eason, E. L. E., Giampapa, M. S., Radick, R. R., Worden, S. P. & Hege, E. K. Spectroscopic and Photometric Observations
552 of a Five-Magnitude Flare Event on UV CETI. *Astron. J.* **104**, 1161 (1992).

553 **41.** Stepanov, A. V. et al. Multifrequency observations of a flare on UV Ceti. *Astron. Astrophys.* **299**, 739 (1995).

554 **42.** Jurić, M. et al. The Milky Way Tomography with SDSS. I. Stellar Number Density Distribution. *Astrophys. J.* **673**,
555 864–914 (2008).

556 **43.** Dhillon, V. S. et al. HiPERCAM: a quintuple-beam, high-speed optical imager on the 10.4-m Gran Telescopio Canarias.
557 *Mon. Not. R. Astron. Soc.* **507**, 350–366 (2021).

558 **44.** Onken, C. A. et al. SkyMapper Southern Survey: Second data release (DR2). *Publ. Astron. Soc. Aust.* **36**, e033 (2019).

559 **45.** Smette, A. et al. Molecfit: A general tool for telluric absorption correction. I. Method and application to ESO instruments.
560 *Astron. Astrophys.* **576**, A77 (2015).

561 **46.** Kausch, W. et al. Molecfit: A general tool for telluric absorption correction. II. Quantitative evaluation on ESO-VLT/X-
562 Shooterspectra. *Astron. Astrophys.* **576**, A78 (2015).

563 **47.** Burgh, E. B. et al. Prime Focus Imaging Spectrograph for the Southern African Large Telescope: optical design. In Iye, M.
564 & Moorwood, A. F. M. (eds.) Instrument Design and Performance for Optical/Infrared Ground-based Telescopes, vol. 4841
565 of Society of Photo-Optical Instrumentation Engineers (SPIE) Conference Series, 1463–1471 (2003).

566 **48.** Kobulnicky, H. A. et al. Prime focus imaging spectrograph for the Southern African large telescope: operational modes. In
567 Iye, M. & Moorwood, A. F. M. (eds.) Instrument Design and Performance for Optical/Infrared Ground-based Telescopes,
568 vol. 4841 of Society of Photo-Optical Instrumentation Engineers (SPIE) Conference Series, 1634–1644 (2003).

569 **49.** Smith, M. P. et al. The prime focus imaging spectrograph for the Southern African Large Telescope: structural and
570 mechanical design and commissioning. In McLean, I. S. & Iye, M. (eds.) Society of Photo-Optical Instrumentation
571 Engineers (SPIE) Conference Series, vol. 6269 of Society of Photo-Optical Instrumentation Engineers (SPIE) Conference
572 Series, 62692A (2006).

573 **50.** Buckley, D. A. H., Swart, G. P. & Meiring, J. G. Completion and commissioning of the Southern African Large Telescope.
574 In Stepp, L. M. (ed.) Society of Photo-Optical Instrumentation Engineers (SPIE) Conference Series, vol. 6267 of Society
575 of Photo-Optical Instrumentation Engineers (SPIE) Conference Series, 62670Z (2006).

576 **51.** Crawford, S. M. et al. PySALT: the SALT science pipeline. In Silva, D. R., Peck, A. B. & Soifer, B. T. (eds.) Observatory
577 Operations: Strategies, Processes, and Systems III, vol. 7737 of Society of Photo-Optical Instrumentation Engineers (SPIE)
578 Conference Series, 773725 (2010).

579 **52.** Sunyaev, R. et al. SRG X-ray orbital observatory. Its telescopes and first scientific results. *Astron. Astrophys.* **656**, A132
580 (2021).

53. Brunner, H. et al. The eROSITA Final Equatorial Depth Survey (eFEDS). X-ray catalogue. *Astron. Astrophys.* **661**, A1 (2022).

54. Arnaud, K. A. XSPEC: The First Ten Years. In Jacoby, G. H. & Barnes, J. (eds.) Astronomical Data Analysis Software and Systems V, vol. 101 of Astronomical Society of the Pacific Conference Series, 17 (1996).

55. CASA Team et al. CASA, the Common Astronomy Software Applications for Radio Astronomy. *Publ. Astron. Soc. Pac.* **134**, 114501 (2022).

56. Hugo, B. V., Perkins, S., Merry, B., Mauch, T. & Smirnov, O. M. Tricolour: An Optimized SumThreshold Flagger for MeerKAT. In Ruiz, J. E., Pierfedereci, F. & Teuben, P. (eds.) Astronomical Society of the Pacific Conference Series, vol. 532 of Astronomical Society of the Pacific Conference Series, 541 (2022).

57. Offringa, A. R. et al. WSCLEAN: an implementation of a fast, generic wide-field imager for radio astronomy. *Mon. Not. R. Astron. Soc.* **444**, 606–619 (2014).

58. Heywood, I. oxkat: Semi-automated imaging of MeerKAT observations (2020).

59. Parsons, S. G. et al. The scatter of the M dwarf mass-radius relationship. *Mon. Not. R. Astron. Soc.* **481**, 1083–1096 (2018).

60. Littlefield, C. et al. Long-term Photometric Variations in the Candidate White-dwarf Pulsar AR Scorpii from K2, CRTS, and ASAS-SN Observations. *Astrophys. J. Lett.* **845**, L7 (2017).

61. Gänsicke, B. T. et al. Cataclysmic variables from a ROSAT/2MASS selection - I. Four new intermediate polars. *Mon. Not. R. Astron. Soc.* **361**, 141–154 (2005).

62. Brown, A. J. et al. Characterizing eclipsing white dwarf M dwarf binaries from multiband eclipse photometry. *Mon. Not. R. Astron. Soc.* **513**, 3050–3064 (2022).

63. Kesseli, A. Y., Muirhead, P. S., Mann, A. W. & Mace, G. Magnetic Inflation and Stellar Mass. II. On the Radii of Single, Rapidly Rotating, Fully Convective M-Dwarf Stars. *Astron. J.* **155**, 225 (2018).

64. Hauschildt, P. H., Allard, F. & Baron, E. The NextGen Model Atmosphere Grid for 3000<=T_{eff}<=10,000 K. *Astrophys. J.* **512**, 377–385 (1999).

65. Knigge, C., Baraffe, I. & Patterson, J. The Evolution of Cataclysmic Variables as Revealed by Their Donor Stars. *Astrophys. J. Suppl. Ser.* **194**, 28 (2011).

66. Stiller, R. A. et al. High-time-resolution Photometry of AR Scorpii: Confirmation of the White Dwarf's Spin-down. *Astron. J.* **156**, 150 (2018).

67. Gaibor, Y., Garnavich, P. M., Littlefield, C., Potter, S. B. & Buckley, D. A. H. An improved spin-down rate for the proposed white dwarf pulsar AR scorpii. *Mon. Not. R. Astron. Soc.* **496**, 4849–4856 (2020).

68. Bédard, A., Bergeron, P., Brassard, P. & Fontaine, G. On the Spectral Evolution of Hot White Dwarf Stars. I. A Detailed Model Atmosphere Analysis of Hot White Dwarfs from SDSS DR12. *Astrophys. J.* **901**, 93 (2020).

612 **69.** Koester, D. White Dwarf Spectra and Atmosphere Models. *arXiv e-prints* arXiv:0812.0482 (2008).

613 **70.** Tremblay, P. E., Bergeron, P. & Gianninas, A. An Improved Spectroscopic Analysis of DA White Dwarfs from the Sloan
614 Digital Sky Survey Data Release 4. *Astrophys. J.* **730**, 128 (2011).

615 **71.** Lauffer, G. R., Romero, A. D. & Kepler, S. O. New full evolutionary sequences of H- and He-atmosphere massive white
616 dwarf stars using MESA. *Mon. Not. R. Astron. Soc.* **480**, 1547–1562 (2018).

617 **72.** Lallement, R. et al. Gaia-2MASS 3D maps of Galactic interstellar dust within 3 kpc. *Astron. Astrophys.* **625**, A135 (2019).

618 **73.** Camisassa, M. E. et al. VizieR Online Data Catalog: Ultra-massive white dwarfs evolution models (Camisassa+, 2019).
619 *VizieR Online Data Catalog* J/A+A/625/A87 (2019).

620 **74.** Marsh, T. R. Doppler Tomography. In Boffin, H. M. J., Steeghs, D. & Cuypers, J. (eds.) Astrotomography, Indirect
621 Imaging Methods in Observational Astronomy, vol. 573, 1 (2001).

622 **75.** Garnavich, P. et al. Driving the Beat: Time-resolved Spectra of the White Dwarf Pulsar AR Scorpii. *Astrophys. J.* **872**, 67
623 (2019).

624 **76.** Schmidtobreick, L. et al. Discovery of Hα satellite emission in a low state of the SW Sextantis star BB Doradus. *Mon. Not.*
625 *R. Astron. Soc.* **422**, 731–737 (2012).

626 **77.** Maxted, P. F. L., Marsh, T. R., Moran, C., Dhillon, V. S. & Hilditch, R. W. The mass and radius of the M dwarf companion
627 to GD448. *Mon. Not. R. Astron. Soc.* **300**, 1225–1232 (1998).

628 **78.** Astropy Collaboration et al. Astropy: A community Python package for astronomy. *Astron. Astrophys.* **558**, A33 (2013).

629 **79.** Price-Whelan, A. M. et al. The Astropy Project: Building an Open-science Project and Status of the v2.0 Core Package.
630 *Astron. J.* **156**, 123 (2018).

631 Correspondence and requests for materials should be addressed to Dr Ingrid Pelisoli (ingrid.pelisoli@warwick.ac.uk).

632 Acknowledgements

633 IP and TRM acknowledge funding by the UK's Science and Technology Facilities Council (STFC), grant ST/T000406/1. IP
634 also acknowledges funding from a Warwick Astrophysics prize post-doctoral fellowship, made possible thanks to a generous
635 philanthropic donation. IP was additionally supported in part by the National Science Foundation under Grant No. NSF
636 PHY-1748958, and thanks the organisers of the KITP Program "White Dwarfs as Probes of the Evolution of Planets, Stars, the
637 Milky Way and the Expanding Universe". SGP acknowledges the support of a STFC Ernest Rutherford Fellowship. VSD and
638 ULTRACAM are funded by the UK's Science and Technology Facilities Council (STFC), grant ST/V000853/1.

639 This research made extensive use of Astropy (http://www.astropy.org) a community-developed core Python package for
640 Astronomy[78,79]

This paper includes data collected by the TESS mission. Funding for the TESS mission is provided by the NASA Explorer Program.

Based in part on observations obtained at the Southern Astrophysical Research (SOAR) telescope, which is a joint project of the Ministério da Ciência, Tecnologia e Inovações do Brasil (MCTI/LNA), the US National Science Foundation's NOIRLab, the University of North Carolina at Chapel Hill (UNC), and Michigan State University (MSU).

The SALT observations were obtained under the SALT Large Science Programme on transients (2021-2-LSP-001; PI: DAHB). Polish participation in SALT is funded by grant No. MEiN nr 2021/WK/01. DAHB and SBP acknowledge researh support by the National Research Foundation.

This work has made use of data from the European Space Agency (ESA) mission *Gaia* (https://www.cosmos.esa.int/gaia), processed by the *Gaia* Data Processing and Analysis Consortium (DPAC, https://www.cosmos.esa.int/web/gaia/dpac/consortium). Funding for the DPAC has been provided by national institutions, in particular the institutions participating in the *Gaia* Multilateral Agreement.

The MeerKAT telescope is operated by the South African Radio Astronomy Observatory (SARAO), which is a facility of the National Research Foundation, an agency of the Department of Science and Innovation. The authors thank SARAO for the award of the MeerKAT Director's Discretionary Time.

This work is based on data from eROSITA, the soft X-ray instrument aboard SRG, a joint Russian-German science mission supported by the Russian Space Agency (Roskosmos), in the interests of the Russian Academy of Sciences represented by its Space Research Institute (IKI), and the Deutsches Zentrum für Luft- und Raumfahrt (DLR). The SRG spacecraft was built by Lavochkin Association (NPOL) and its subcontractors, and is operated by NPOL with support from the Max Planck Institute for Extraterrestrial Physics (MPE). The development and construction of the eROSITA X-ray instrument was led by MPE, with contributions from the Dr. Karl Remeis Observatory Bamberg & ECAP (FAU Erlangen-Nuernberg), the University of Hamburg Observatory, the Leibniz Institute for Astrophysics Potsdam (AIP), and the Institute for Astronomy and Astrophysics of the University of Tübingen, with the support of DLR and the Max Planck Society. The Argelander Institute for Astronomy of the University of Bonn and the Ludwig Maximilians Universität Munich also participated in the science preparation for eROSITA. The eROSITA data shown here were processed using the eSASS/NRTA software system developed by the German eROSITA consortium.

Support of the Deutsche Forschungsgemeinschaft (DFG) under grant number 536/37-1 is gratefully acknowledged.

Author contributions

All authors contributed to the work presented in this paper. IP wrote the manuscript and lead the follow-up and analysis of the system, with significant input from TRM. DAHB carried out follow-up observations at SAAO and contributed to analysis of the optical data. IH carried out reduction and analysis of the radio data. SBP carried out follow-up observations at SAAO and the analysis and modelling of polarimetric data. A. Schwope and A. Standke obtained and analysed the X-ray data. PAW obtained

673 the radio data. SGP and MJG contributed to initial identification and analysis of the system. SOK, JM, and ADR contributed
674 to observational follow-up. EB, AJB, VSD, MJD, PK, SPL, DIS, and JFW contributed to the maintenance of operations of
675 ULTRACAM.

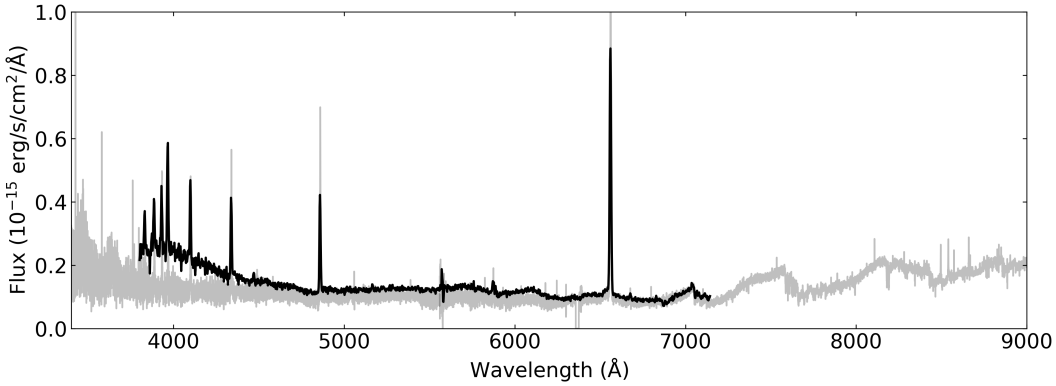

Extended Data Figure 1. Optical spectrum of J1912−4410. The black line shows the SOAR spectrum obtained for J1912−4410, which confirmed its spectral characteristics to be similar to AR Sco. The grey line shows X-Shooter spectra from the UVB and VIS arms obtained around the same orbital phase as the SOAR spectrum (0.85). The flux calibration of the SOAR spectrum is poor towards the blue due to reduced sensitivity.

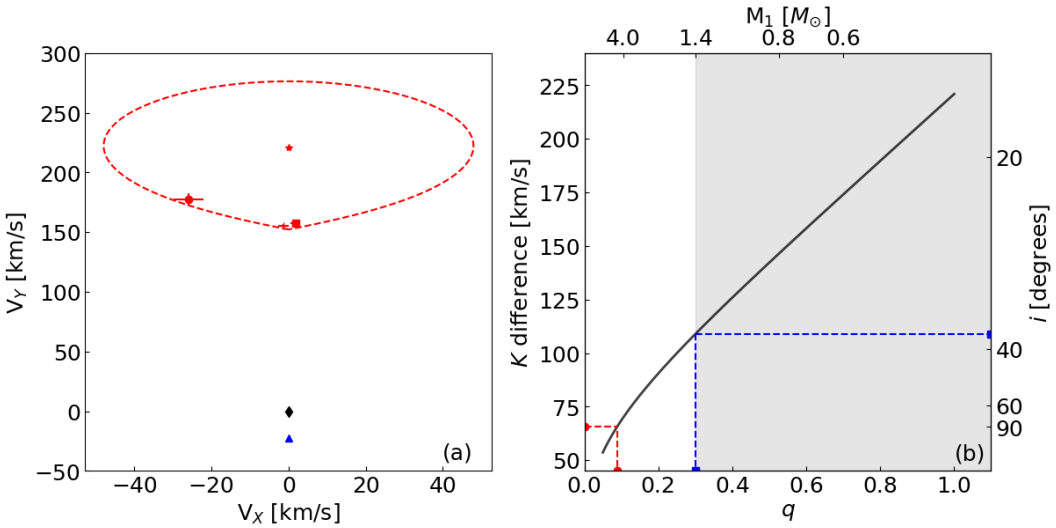

Extended Data Figure 2. Constraints from Roche geometry. In panel (a) the star marks measurements from the NaII line (by our definition the centre of mass of the M-dwarf). The circle, cross, and square mark respectively Hα, Hβ, and Hγ, which were fitted as $V = \gamma - V_X \cos(2\pi\phi) + V_Y \sin(2\pi\phi)$, where ϕ is the orbital phase and γ, the systemic velocity, was kept fixed to the previously determined value. Hβ, and Hγ give consistent measurements, whereas Hα seems to trail the leading face of the M-dwarf. The red dashed line is the Roche lobe of the M-dwarf for $q = 0.1$. The black dot and blue diamond mark the centre of mass of the system and of the white dwarf, respectively. The black line in panel (b) shows the expected difference between the irradiated face and centre of mass radial velocity semi-amplitudes as a function of q, assuming the M-dwarf fills its Roche lobe. The right-hand y-axis shows the required inclination to explain the detected K difference. The observed value of K difference sets a minimum for q, which would happen if the system was seen at 90° inclination, as indicated by the red dashed line. The area shaded in grey corresponds to M_1 values consistent with a white dwarf for a Roche lobe-filling companion, and implies the minimum q value of 0.3. This minimum q corresponds to a maximum inclination of 37° (blue dashed lines).

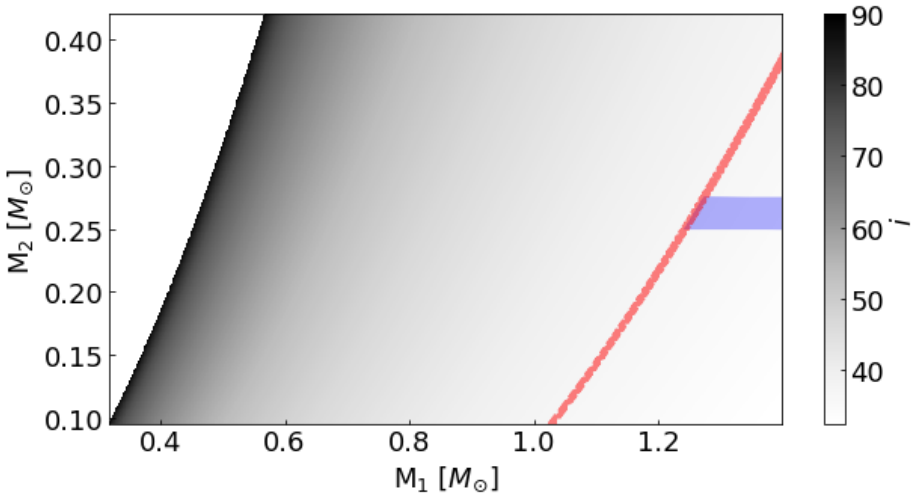

Extended Data Figure 3. Constraints from the binary mass function. The colour map shows the required inclination to explain the observed K_2 for given values of M_1 and M_2 shown in the x- and y-axis. The red line marks the maximum inclination of 37°, derived from Roche geometry, and the blue shaded area indicates the M_2 mass derived from a mass-radius relationship. Given the high systematic uncertainty on M_2, we adopt less strict constraints of $M_1 = 1.2 \pm 0.2$ M$_\odot$ and $M_2 = 0.25 \pm 0.05$ M$_\odot$.

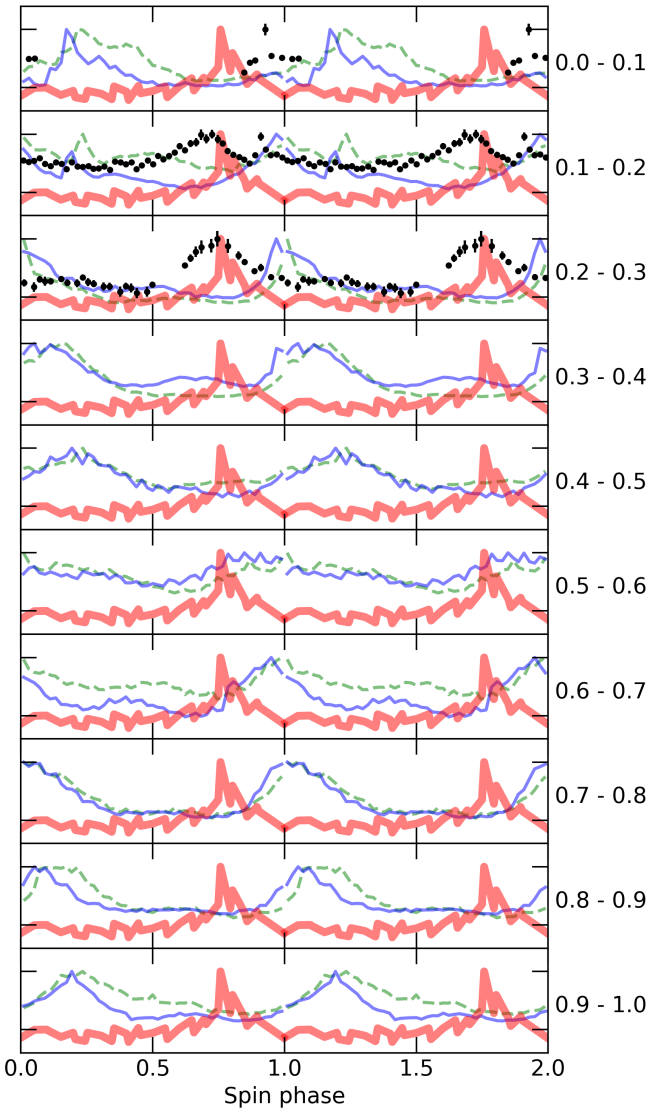

Extended Data Figure 4. Pulse shape for different orbital phases and nights. The thick red line shows all the X-ray data averaged and folded on the spin ephemeris. The thin lines and symbols show ULTRACAM g_s data averaged and folded on the same ephemeris, but considering data only within the orbital phase ranges shown on the right of the plot. The green dashed line shows data taken on 2022 June 07, the black symbols are data taken on 2022 September 17 (simultaneously with the X-ray data), and the solid blue line shows data for 2022 September 23. All data were normalised to the strongest peak to facilitate comparison. As also seen in Fig. 2, the peak of the X-ray pulses does not align with the bulk of optical pulses. However, it does align with the optical peaks observed on 2022 September 17. This difference cannot be attributed to uncertainty in the ephemeris, given the agreement between data taken on nights before and after the X-ray observations. Additional simultaneous data is needed to determine the cause of misalignment, which could possibly be due to sporadic changes on pulse profile.

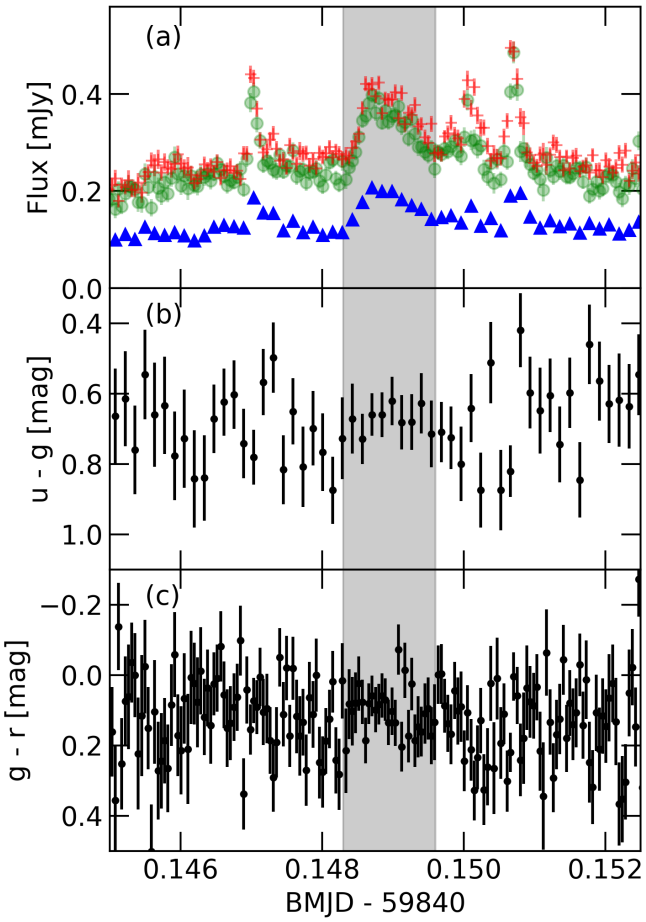

Extended Data Figure 5. Flux and colour of the possible flare. Panel (a) shows the flux in the u_s (blue triangles), g_s (green circles), and r_s (red crosses) bands in the region of the feature that we identify as a flare (marked by the shaded grey area). Panels (b) and (c) show the $u_s - g_s$ and $g_s - r_s$ colours. Unlike typical M-dwarf flares, there is no evidence of flux increase towards the blue.

Supplementary Information

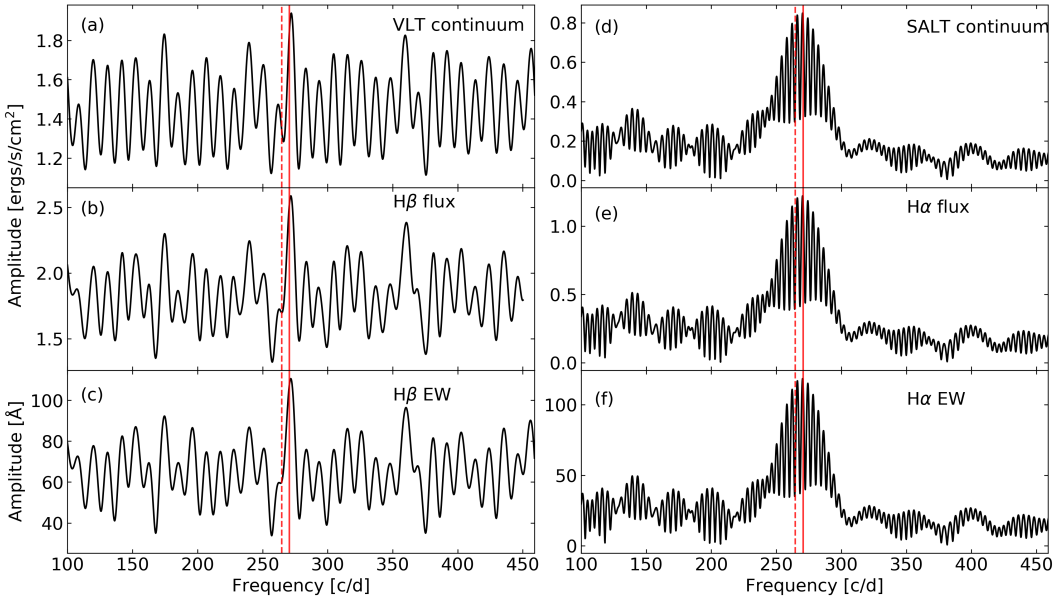

Supplementary Figure 1. Fourier transforms of data derived from spectroscopy. Panels (a)-(c) show Fourier transforms of the continuum, Hβ flux, and Hβ equivalent width derived from VLT/X-shooter spectra. Panels (d)-(f) show the same but for Hα and SALT spectra. For the continuum, flux was integrated over the spectrum masking the line regions, whereas only the lines themselves were integrated when obtaining the line flux. The solid line shows the spin frequency, whereas the dashed line shows beat frequency $\omega - \Omega$.

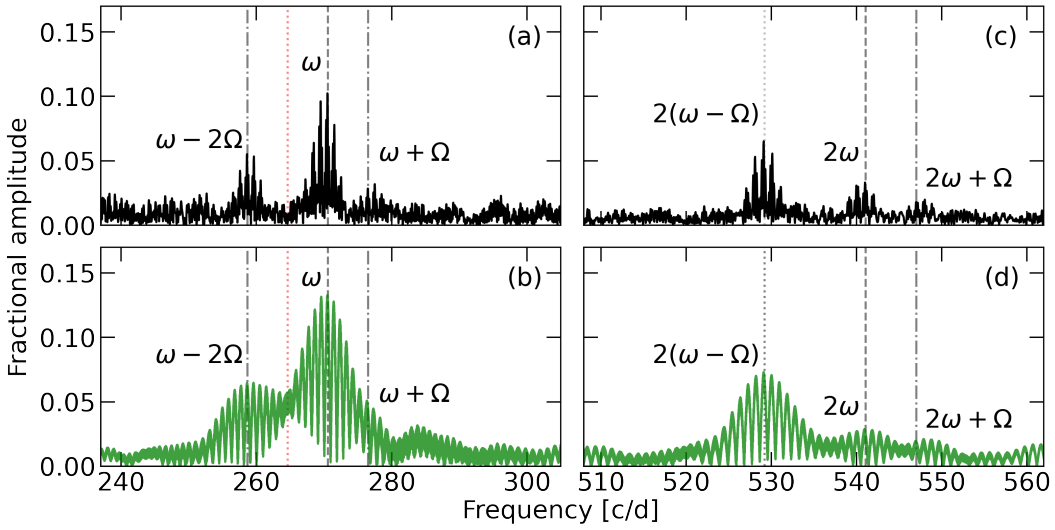

Supplementary Figure 2. Fourier transforms of HIPPO and ULTRACAM g_s. The left panels show the Fourier transform of HIPPO data (a) and ULTRACAM g_s (b) around the spin frequency ω. Other peaks also visible are labelled. The beat frequency $\omega - \Omega$ (red dotted line) is not detected. The right panels show the same Fourier transforms around the first harmonic of the spin frequency, showing that the first harmonic of the beat frequency is detected and even dominant over the spin harmonic.

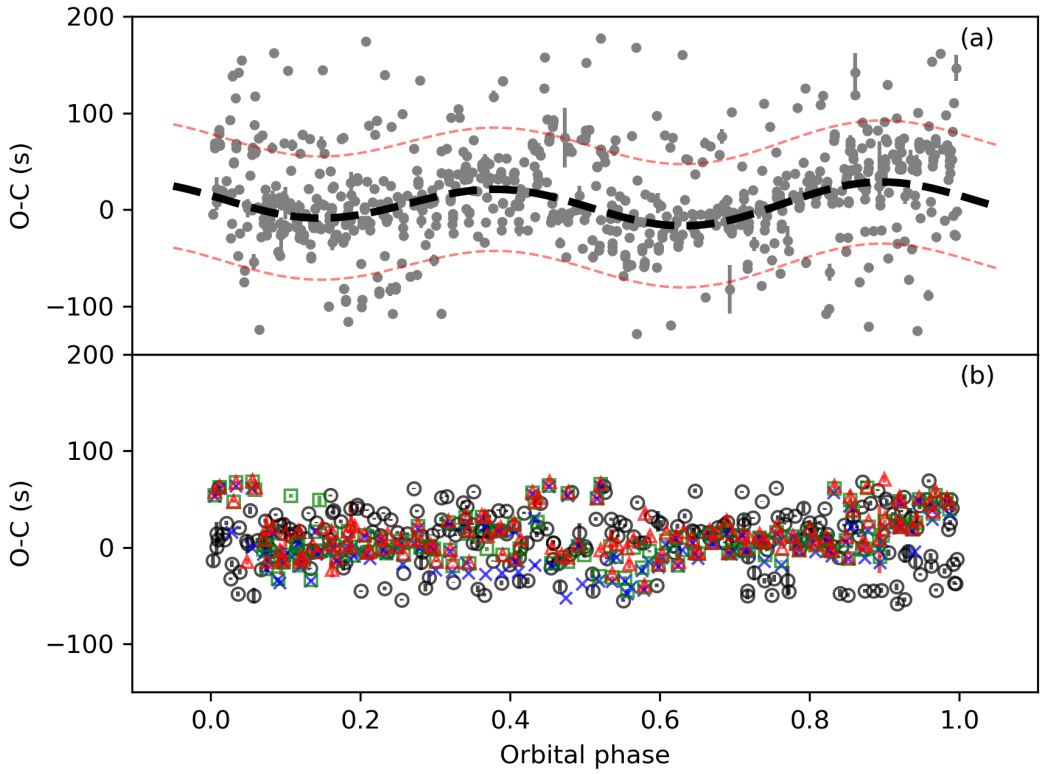

Supplementary Figure 3. Residuals from linear fit. Panel (a) shows the residuals as a function of orbital phase after an initial linear fit to the pulse arrival times derived from ULTRACAM and HIPPO data. There is modulation with orbital phase, modelled by a Fourier series shown by the black dashed line. The red dashed lines show the same model plus or minus 0.25 cycles; points below or above the red lines were excluded from the final fit. Panel (b) shows the residuals after the fit that resulted in the ephemeris of Equation 6. In panel (b) the symbols are grey circles for HIPPO data, red triangles for ULTRACAM r_s and i_s data, green squares for ULTRACAM g_s, and blue crosses for ULTRACAM u_s.

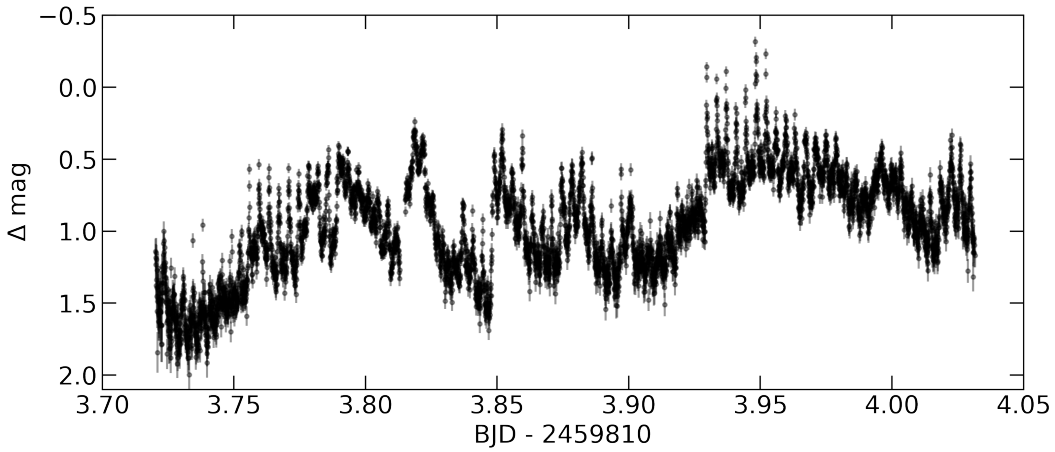

Supplementary Figure 4. Optical light curve showing possible flaring. Light curve of J1912−4410 taken with the Mookodi instrument on the SAAO 1-m Lesedi telescope on 2022 August 21. There are strong changes in amplitude, e.g. between BJD 2459813.8 and 2459813.85, which are suggestive of flaring.

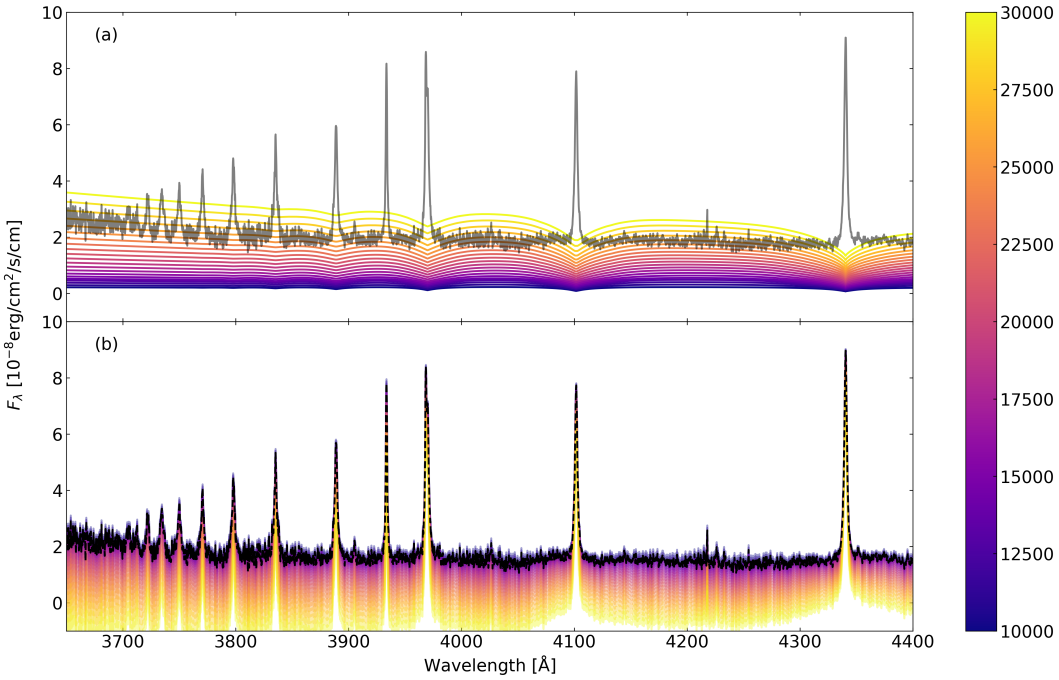

Supplementary Figure 5. Constraining the temperature of the white dwarf. Panel (a) shows in grey a spectrum obtained by co-adding all UVB spectra taking around minimum flux. Model white dwarf spectra with $\log g = 8.50$ and different effective temperatures, indicated by the colour bar, are shown. The models were scaled taking J1912−4410's distance into account and assuming a white dwarf radius from cooling models for $\log g = 8.50$. In panel (b), the model white dwarf spectra were subtracted from the observed spectrum. For the correct white dwarf model, this should simply remove the white dwarf contribution, and add no new features. From a certain temperature, the strength of the lines in the model is such that the subtraction visibly adds broad features to the spectrum. By numerically determining when that happens, we placed an upper limit on the white dwarf temperature of 13 000 K.

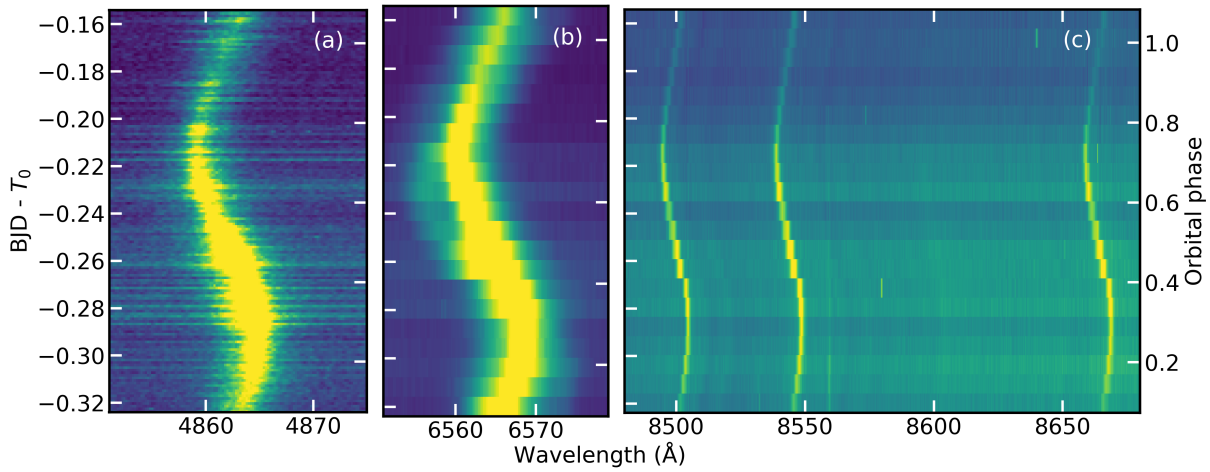

Supplementary Figure 6. Trailed spectra of J1912−4410. Panel (a) shows spectra taken with X-shooter's UVB arm, around Hβ. Panels (b) and (c) show data from the VIS arm, around Hα and the CaII triplet, respectively. The left hand axis shows time in BJD, and the right hand axis shows orbital phases for all panels. For Hβ, the integration time was short enough to resolve the pulsations, which can be seen in the continuum.

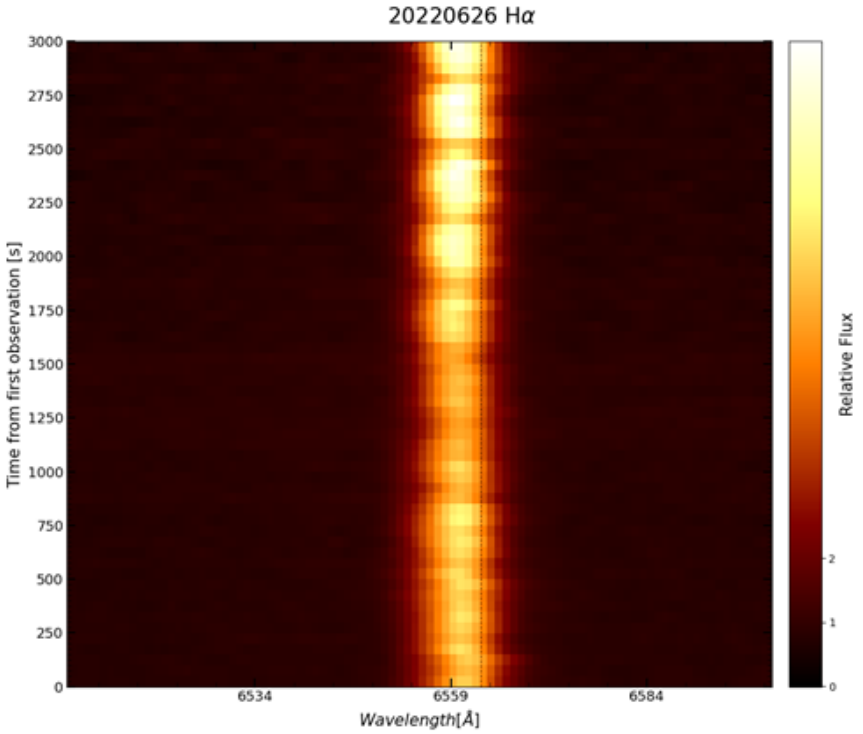

Supplementary Figure 7. Trailed Hα spectra. Trail of spectra obtained via frame-transfer spectroscopy with SALT. The pulsed behaviour of Hα can be clearly seen in the flux changes, in particular towards the end of observations (top of the plot).

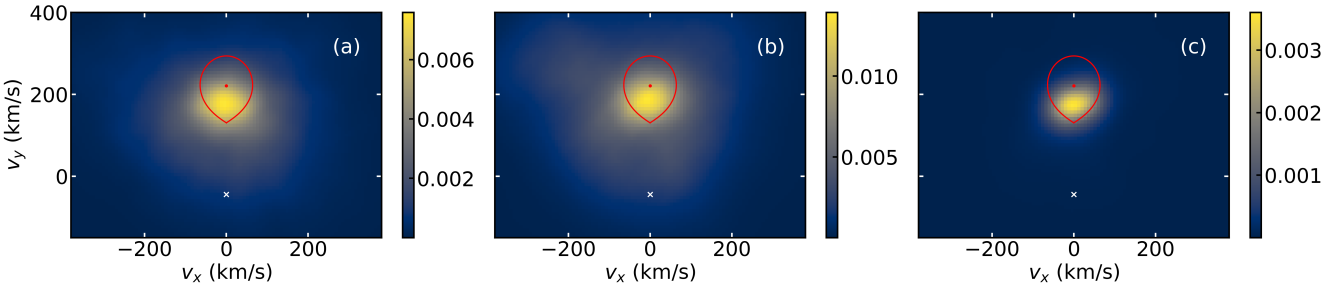

Supplementary Figure 8. Doppler tomography of J1912−4410. Doppler tomography of the Hβ (panel a), Hα (panel b) and Ca II triplet (panel c) lines. The white cross marks the position of the white dwarf, the red line indicates the Roche lobe of the companion assuming $q = 0.2$, and the red dot its centre of mass. **The colour bars show emission intensity after normalising and subtracting the continuum.**

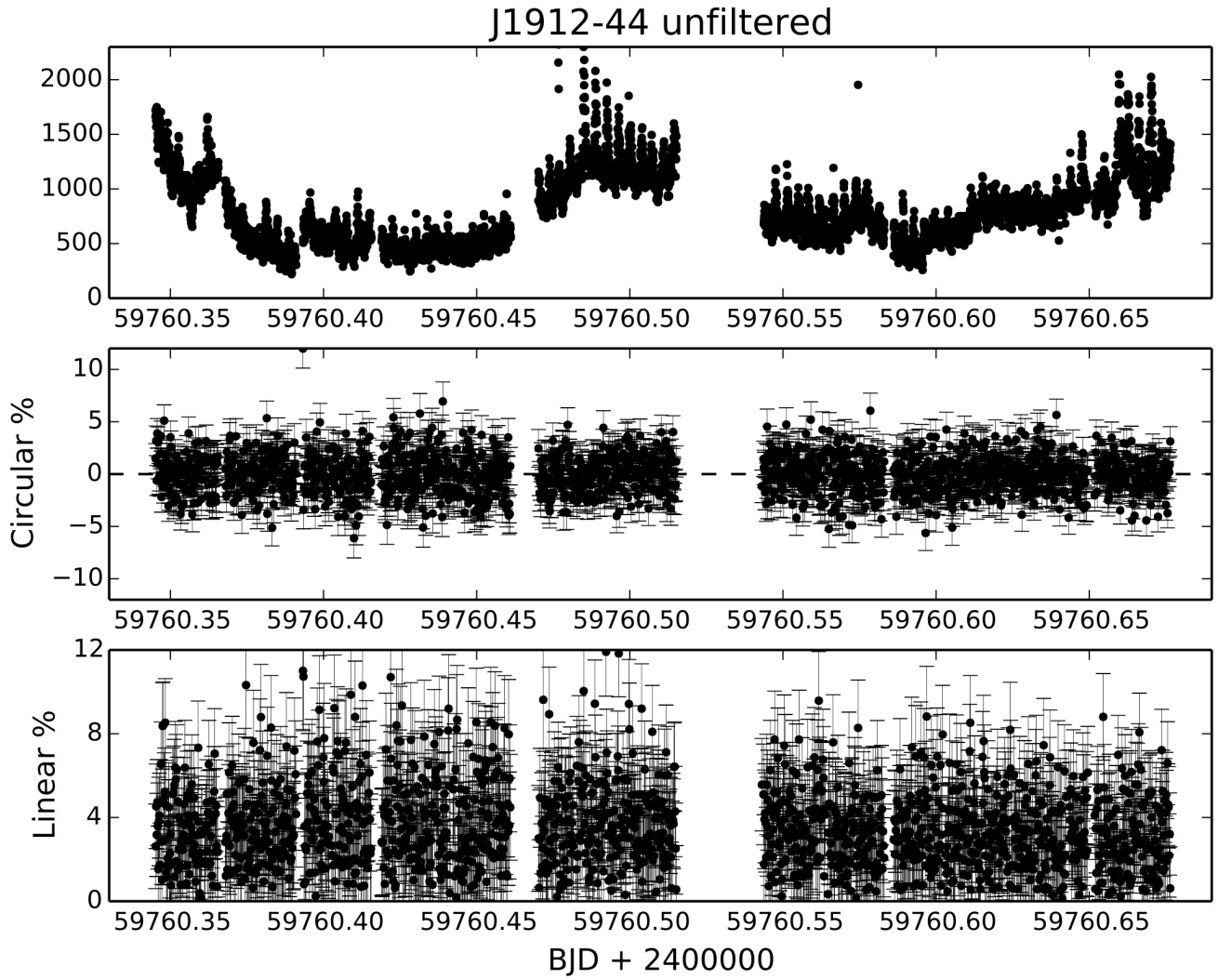

Supplementary Figure 9. Example HIPPO photo-polarimetry of J1912−4410 from 29 June 2022. Top to bottom show the photometry, circular polarisation and linear polarisation respectively.

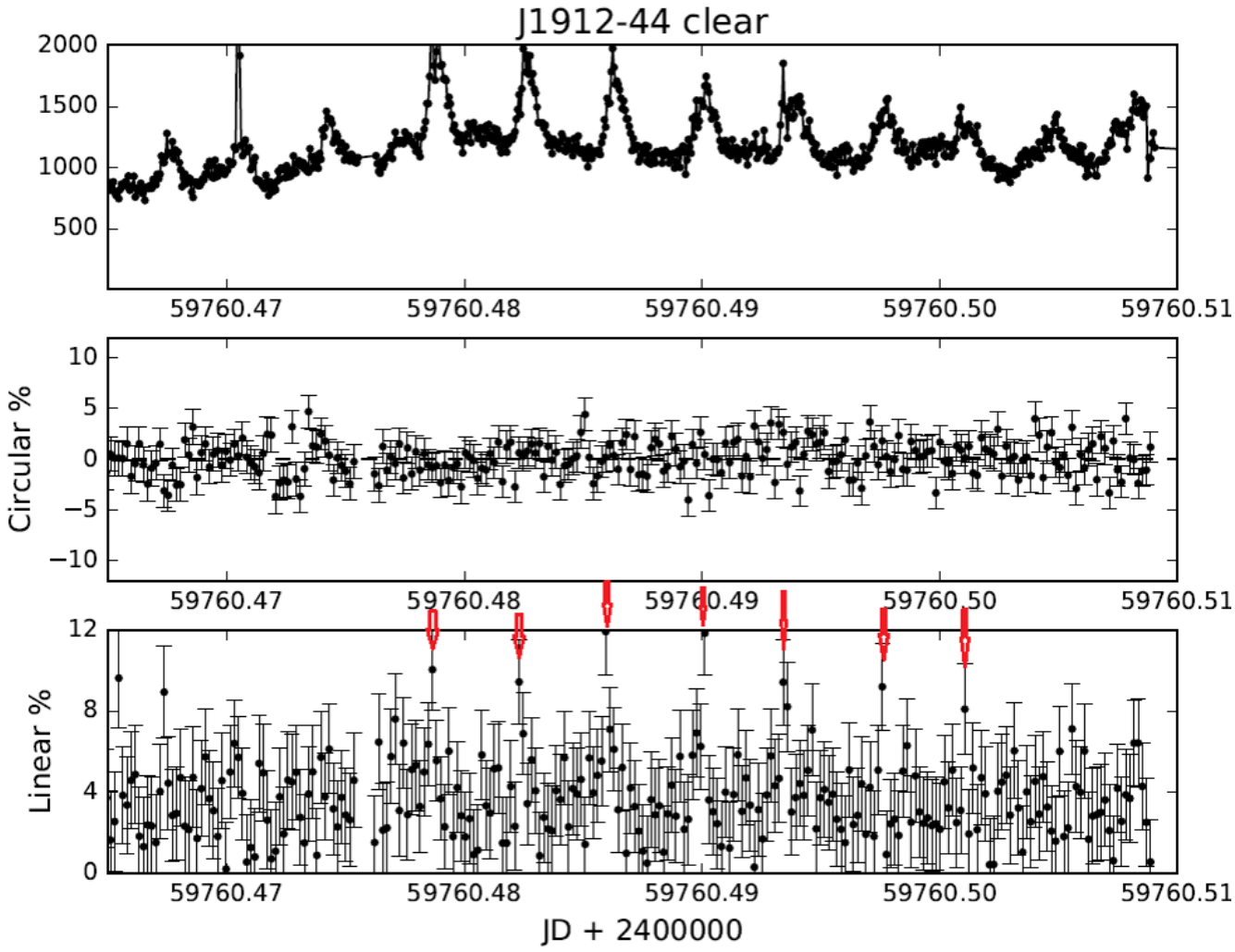

Supplementary Figure 10. Zoomed in region of Supplementary Figure 9 highlighting the linear polarisation pulses. Top to bottom show the photometry, circular polarisation and linear polarisation respectively.

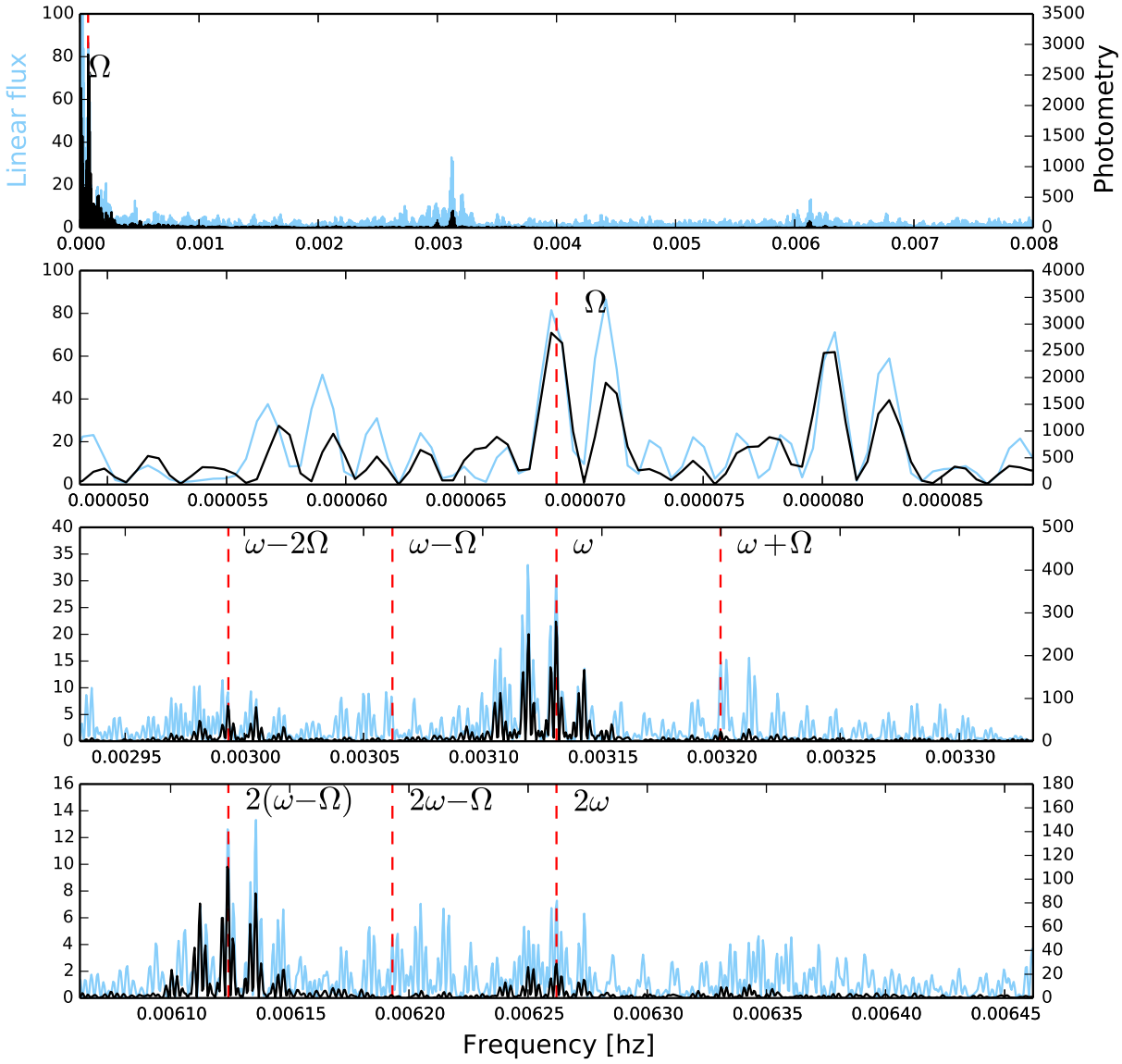

Supplementary Figure 11. Fourier transforms of HIPPO photometry and linear polarimetry. Black is photometry, lightskyblue is linear polarised flux.

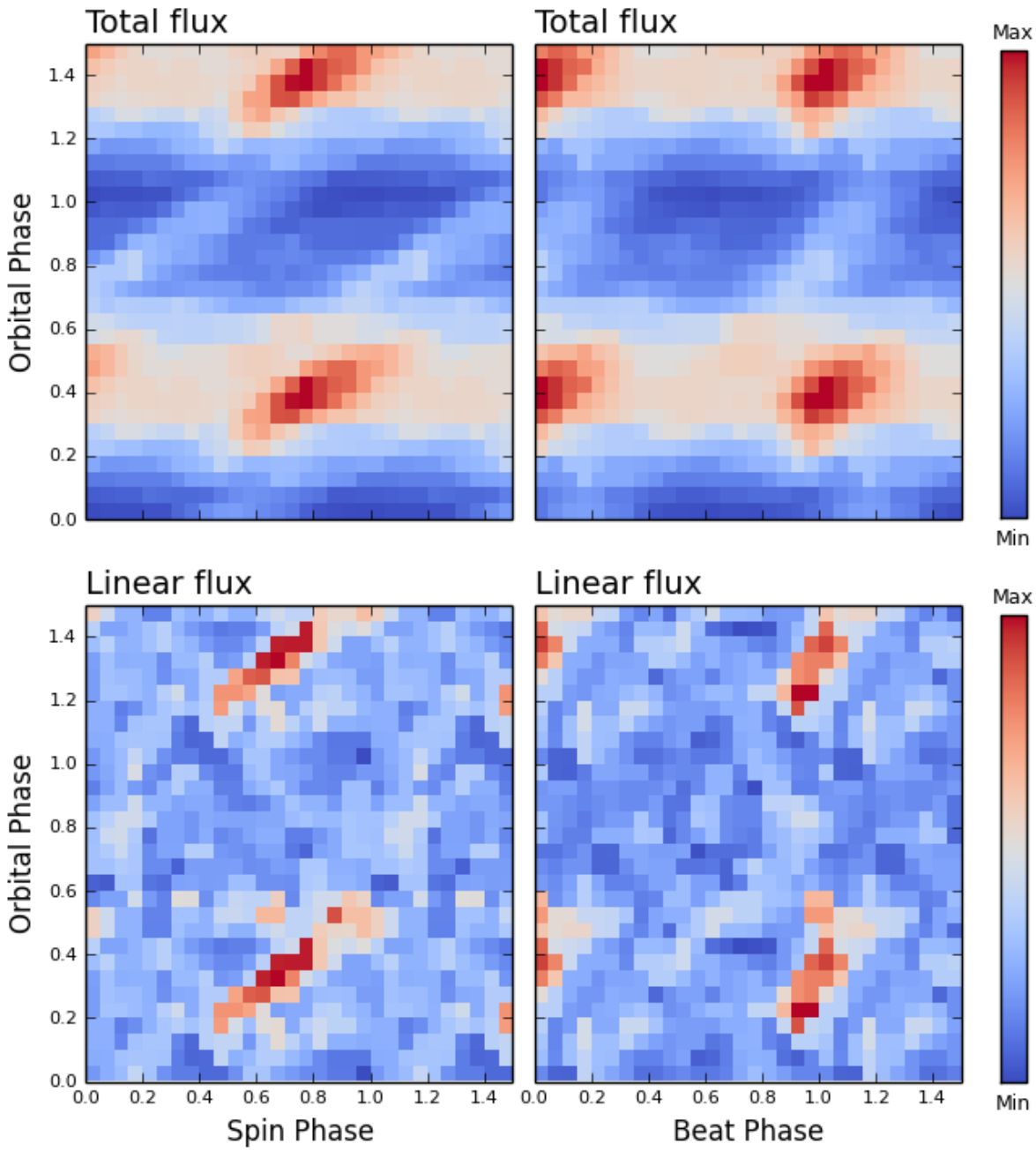

Supplementary Figure 12. Photopolarimetry of J1912-4410 assuming beat to be the dominant frequency. Panels show the same as in Figure 4, but assuming beat rather than the spin as the dominant frequency, which results in considerable smearing.

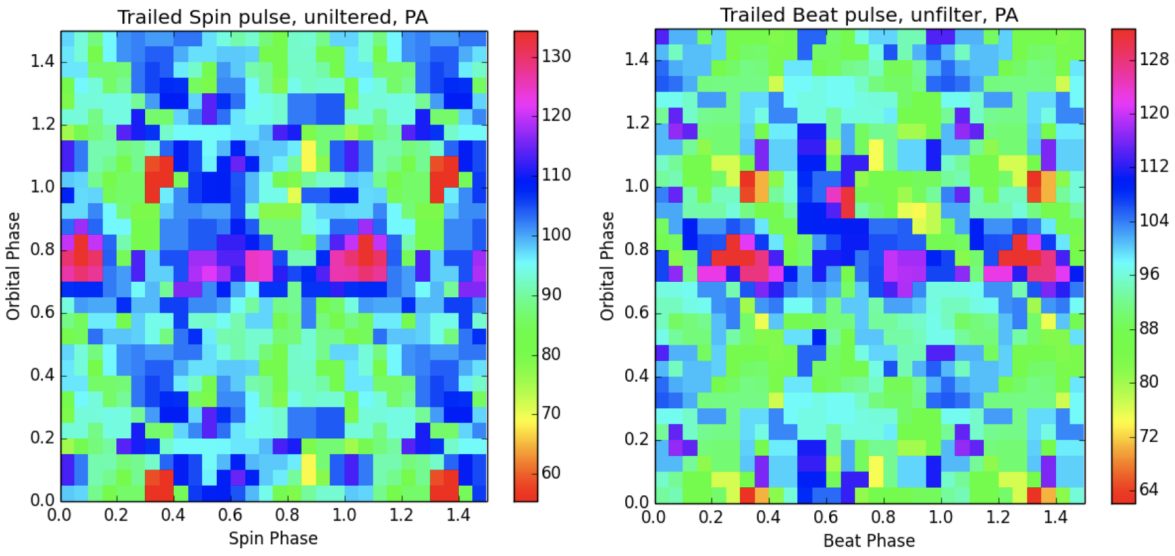

Supplementary Figure 13. Position angle of the linear polarisation as a function of orbital and spin/beat phases. The left panel shows the position angle when the dominant frequency is assumed to be the spin, while the right shows the same when the beat is assumed to be dominant. In the left panel, there is a hint of a consistent angle for orbital phase ≈ 0.45.